GENETICS

Release of CHK-2 from PPM-1.D anchorage schedules meiotic entry

Antoine Baudrimont[1], Dimitra Paouneskou[1]†, Ariz Mohammad[2]†, Raffael Lichtenberger[3], Joshua Blundon[4], Yumi Kim[4], Markus Hartl[5], Sebastian Falk[3], Tim Schedl[2], Verena Jantsch[1]*

Transition from the stem/progenitor cell fate to meiosis is mediated by several redundant posttranscriptional regulatory pathways in *Caenorhabditis elegans*. Interfering with all three branches causes tumorous germ lines. SCF[PROM-1] comprises one branch and mediates a scheduled degradation step at entry into meiosis. *prom-1* mutants show defects in the timely initiation of meiotic prophase I events, resulting in high rates of embryonic lethality. Here, we identify the phosphatase PPM-1.D/Wip1 as crucial substrate for PROM-1. We report that PPM-1.D antagonizes CHK-2 kinase, a key regulator for meiotic prophase initiation, including DNA double-strand breaks, chromosome pairing, and synaptonemal complex formation. We propose that PPM-1.D controls the amount of active CHK-2 via both catalytic and noncatalytic activities; notably, noncatalytic regulation seems to be crucial at meiotic entry. PPM-1.D sequesters CHK-2 at the nuclear periphery, and programmed SCF[PROM-1]–mediated degradation of PPM-1.D liberates the kinase and promotes meiotic entry.

INTRODUCTION

Transition from the dividing stem/progenitor cell fate to meiosis is a key step in producing gametes (*1*). In the germ line, this crucial differentiation step is governed by three parallel pathways involved in posttranscriptional gene regulation in *Caenorhabditis elegans*. These are the defective in Germ Line Development-1 (GLD-1), GLD-2, and Skp1-cullin-F-box protein PRogression Of Meiosis-1 (SCF[PROM-1]) pathways that act by translational repression, polyadenylate tail–mediated translational activation and targeted protein degradation, respectively (fig. S1) (*2*). The pathways operate redundantly, which means that only double mutants interfering with at least two pathway branches lead to hyperproliferative germ lines and failure in meiotic entry. Triple mutants affecting all three pathways produce highly tumorous germ lines with little or no expression of meiotic markers (*2*). In the progenitor zone, where cells undergo mitotic cell cycling and premeiotic replication, the activities of the three pathways required for meiotic entry are down-regulated by abnormal Germ Line Proliferation-1 (GLP-1)/Notch signaling (*2*, *3*).

The continuous replenishment of meiocytes through divisions in the progenitor zone displaces cells proximally at a rate of approximately 1 cell row/hour through the germ line (*4*). After one round of meiotic S phase, cells enter prophase of meiosis I (leptonema, zygonema, pachynema, diplonema, and diakinesis), which is organized as a spatiotemporal meiotic time course and can be visualized in the dissected gonads of *C. elegans* hermaphrodites (*5*). The generation of gametes via meiosis requires two divisions. In meiosis I, parental homologous chromosomes (one from each parent) are separated, and in meiosis II, each chromosome splits into its two sister chromatids.

The physical linkage between homologs aids their correct segregation. This linkage is a result of programmed induction of DNA double-strand breaks (DSBs); pairwise alignment of the homologous chromosomes, which are organized in loops tethered to the meiotic chromosome axis; installation of the synaptonemal complex (SC) between the paired homologs; and repair of the DSBs using a chromatid of the parental homolog via homologous recombination (*6*). A further highly conserved feature in prophase of meiosis is the vigorous movements of chromosomes, which promote the pairwise alignment of the homologous chromosomes and installation of the SC between them (*7*). The prophase events must be coordinated to achieve normal disjunction at the meiotic divisions.

prom-1 mutants show defects in the timely and coordinated initiation of these events (*8*). The mutants have an extended meiotic entry zone, characterized by the presence of meiotic cohesion, chromosome axes, and SC proteins as polycomplexes, indicating that the proteins are produced and awaiting assembly onto chromosomes. Furthermore, despite the apparent completion of meiotic S phase, DSB induction and repair and all signs of prophase chromosome movements are delayed. These pleiotropic defects result in a mix of univalent and bivalents, which leads to chromosome mis-segregation, a high incidence of male progeny, and high embryonic death (*8*).

In *C. elegans*, the DNA damage signaling kinase CHeckpoint Kinase-2 (CHK-2) acts as a key regulator of prophase meiotic processes. *chk-2* mutants are defective in DSB induction, SC formation, and chromosome movements and lack meiotic feedback control that permits bivalent formation (*9*–*17*). The inner nuclear envelope protein S. pombe sad1/Ce-UNC-84-1 (SUN-1), which is involved in the chromosome movements, is a prominent substrate of CHK-2. Phosphorylated SUN-1 serine-8 [SUN-1(S8Pi)] in the nuclear interior marks meiotic entry (*10*) and was used as a marker for CHK-2 kinase activity throughout this study. Fundamentally different from the *prom-1* mutants, *chk-2* mutants show normal chromosome axis morphogenesis (*18*).

prom-1 encodes an F-box protein homologous to human FBXO47 (*8*, *19*). Together with a cullin and an RING-box protein 1 (Rbx) protein, PROM-1 forms part of a multisubunit E3 ubiquitin ligase complex (called SCF) (*20*), which mediates recognition and binding

[1]Department of Chromosome Biology, Max Perutz Labs, University of Vienna, Vienna BioCenter, Vienna, Austria. [2]Department of Genetics, Washington University School of Medicine, St. Louis, MO, USA. [3]Department of Structural and Computational Biology, Max Perutz Labs, University of Vienna, Vienna BioCenter, Vienna, Austria. [4]Department of Biology, Johns Hopkins University, Baltimore, MD, USA. [5]Mass Spectrometry Facility, Max Perutz Labs, Vienna BioCenter, Vienna, Austria.
*Corresponding author. Email: verena.jantsch@univie.ac.at
†These authors contributed equally to this work.

of the E2 ubiquitin–conjugating enzyme to the substrate; the substrate is consequently targeted for degradation. We still do not have a comprehensive picture of which proteins need to be subjected to the programmed degradation step at the transition between the stem/progenitor cell fate and meiotic differentiation. Whereas the cyclin, CYclin E-1 (CYE-1), has been identified as one of the targets of SCF[PROM-1], *cye-1* inactivation failed to suppress the pronounced meiotic entry delay seen in *prom-1* mutant worms (*2*).

In this study, we report the identification of protein phosphatase, Mg^{2+}/Mn^{2+} dependent 1D (*ppm-1.D*) as a potent suppressor of the embryonic lethality associated with the *prom-1* mutants. In the double mutants, *prom-1* defects in meiotic entry are largely reversed, and key meiotic processes of prophase I are restored. *ppm-1.D* encodes a serine/threonine phosphatase in the protein phosphatase 2C (PP2C) family that is orthologous to human *PPM1D* (formally known as *WIP1*). We provide evidence that PPM-1.D acts as an antagonizing phosphatase to the meiotic regulator CHK-2, which it keeps in an inactive state in the progenitor zone compartment through a non-catalytic sequestration mechanism. Nevertheless, PPM-1.D regulates meiotic entry via both catalytic and noncatalytic activities, and therefore, *ppm-1.D* null mutants display features of premature meiotic entry. Thus, we present a previously undescribed role for the PPM-1.D phosphatase, in addition to its known involvement in

the response to DNA damage in somatic cells (*21*). This study provides a rationale to test whether human PPM1D is also a substrate for degradation by the human PROM-1 F-box protein homolog, FBXO47, of which mutations in the encoding gene have been associated with renal carcinoma (*19*). Furthermore, *PPM1D* is often up-regulated in cancer cells (*21*).

RESULTS

Identification of *ppm-1.D* as a *prom-1* target

prom-1 encodes an F-box protein and is part of the SCF E3 ubiquitin ligase complex, which targets substrate proteins for degradation by the proteasome (Fig. 1A) (*2*, *8*, *20*). We tagged PROM-1 at its C terminus and examined its expression levels throughout the *C. elegans* germ line (see table S1 for functionality of the tagged line). We costained PROM-1::hemagglutinin with the cohesion regulator Drosophila Wings APart-Like cohesin interactor-1, which showed characteristic nuclear staining in the progenitor zone with a pronounced drop at meiotic entry (Fig. 1B, left, cyan) (*22*). Quantification of the normalized signal intensity of PROM-1 revealed that it started to rise at ~10 cell diameters (rows) from the distal tip of the germ line and reached its maximum level at ~20 cell diameters from the distal tip (Fig. 1B, right). The peak is ~20 fold above basal level
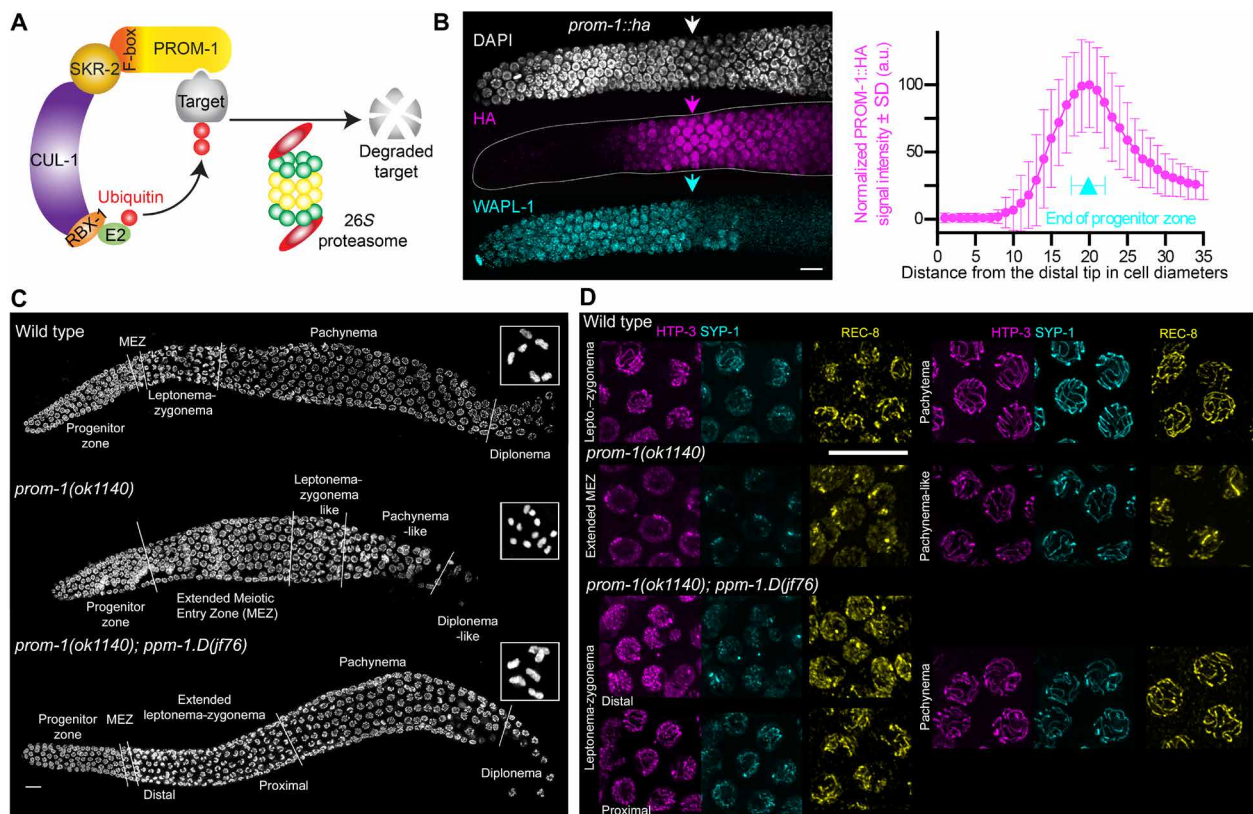
Fig. 1. Loss of SCF[PROM-1] activity at meiotic entry is rescued by mutating *ppm-1.D*. (**A**) Schematic diagram of the SCF[PROM-1] complex. (**B**) Left: Immunodetection of WAPL-1 (cyan) and PROM-1::HA (magenta) in the progenitor zone, at the distal end of the *C. elegans* germ line. Arrows mark the entry into meiosis, which occurs at the leptonema-zygonema. Scale bar, 5 μm. Right: Normalized levels of PROM-1::HA (magenta) throughout the progenitor cell zone, measured as cell diameters from the distal tip; the end of the progenitor zone (cyan) is marked. Error bars, SD. DAPI, 4′,6-diamidino-2-phenylindole; a.u., arbitrary units. (**C**) Gonads displaying prophase I for the indicated genotypes. Scale bar, 10 μm. Boxed insets show representative diakinesis chromosomes. (**D**) Insets showing staining for HTP-3 (magenta), SYP-1 (cyan), and REC-8 (yellow) for the depicted zones. Scale bar, 10 μm.

in the distal-most germ cells and coincides with the end of the progenitor zone, marked by WAPL-1 (Fig. 1B, right, cyan triangle). The increase in the levels of PROM-1 coincident with meiotic entry suggests the presence of targets for regulated degradation to promote entry into meiosis, consistent with the *prom-1* mutant phenotype characterized by an extended meiotic entry zone (*8*).

To identify targets of SCF^PROM-1, we conducted a suppressor screen to search for mutants that would rescue the low viability phenotype of *prom-1(ok1140)* (4 ± 1%, *n* = 9 hermaphrodites; see Materials and Methods and fig. S2A). We isolated the *jf76* allele, which mapped to the *ppm-1.D* gene. Combining *jf76* with *prom-1* led to a notably improved hatch rate of 41 ± 9% (*n* = 10 hermaphrodites; fig. S2B).

Further cytological examination of the double mutant *prom-1(ok1140); ppm-1.D(jf76)* revealed three outcomes: first, the timely restoration of the appearance of leptonema-zygonema after the meiotic entry zone [comprising two to three nuclear cell rows in the wild type, where SC proteins have been expressed but are not yet loaded onto chromosomes (*8*)], contrasting the extended meiotic entry zone in *prom-1(ok1140)* (Fig. 1C) and, second, the loading of the meiotic cohesin RECombination abnormal-8 (REC-8) and chromosome axial proteins [as shown for Him-Three Paralog-3 (HTP-3) (*23*)] and extension of the SC [as shown for SYnaPsis in meiosis abnormal-1 (SYP-1); Fig. 1D (*24*, *25*)]. We noticed that in the double mutant, the transition zone (comprising leptonema and zygonema) was

prolonged and that HTP-3, SYP-1, and REC-8 persisted longer in aggregates than in the wild type. Nevertheless, at the proximal end of the transition zone, the chromosome axes and the SC appeared to be fully decorated with the relevant markers (Fig. 1D). Third, six bivalents were formed compared with the mixture of univalent and bivalents seen in the *prom-1(ok1140)* single mutant (Fig. 1C, insets). Consistent with the efficient formation of bivalents, pairing of homologous chromosomes and RADiation sensitivity abnormal/yeast RAD-related-51 (RAD-51) loading were restored to wild-type levels in the *prom-1(ok1140); ppm-1.D(jf76)* double mutant (fig. S2, C and D). In summary, we showed that PROM-1 protein levels peak at meiotic entry and that the *ppm-1.D(jf76)* mutant can efficiently suppress the *prom-1* phenotype, as evidenced by the restoration of high hatch rates for embryos laid by the double mutant.

PPM-1.D encodes a conserved PP2C phosphatase, and protein abundance is regulated by the SCF^PROM-1 complex

The *ppm-1.D* gene is conserved from *C. elegans* to humans (Fig. 2A) and is known to be involved in the DNA damage response in mammals (*26*). PPM1D is a chromatin-bound phosphatase that targets gamma H2A histone family member X (γH2AX), Ataxia Telangiectasia Mutated (ATM), Chk1, Chk2, Mouse double minute 2 homolog (MDM2), and p53 and reverses the effects of ATM-dependent mitotic cell cycle arrest triggered by DNA damage. In animal cells, the
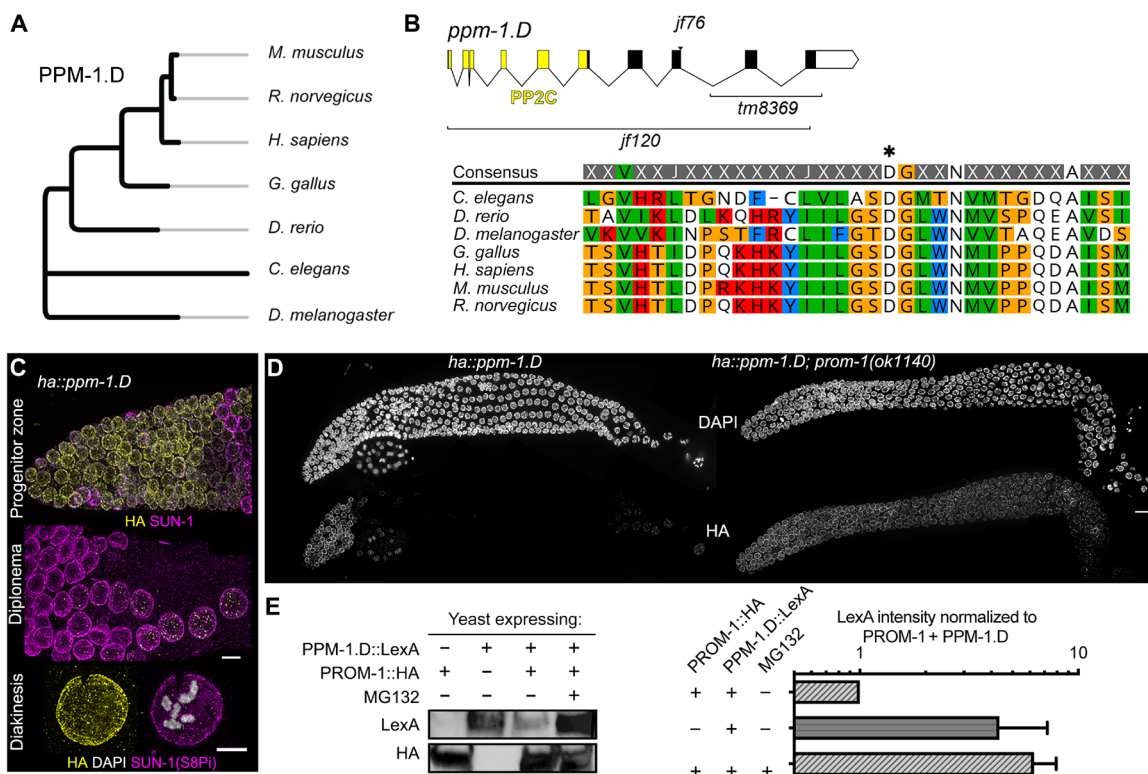
Fig. 2. PPM-1.D is a conserved PP2C phosphatase and its expression is controlled by SCF^PROM-1. (**A**) Phylogenetic tree of PPM-1.D. (**B**) Gene structure of *ppm-1.D*, with domains, exons/introns, and alleles depicted (top) and alignment of PPM-1.D protein sequences (bottom; amino acid range, 498 to 530) for selected organisms to highlight conservation of the PP2C domain. Asterisk marks the conserved aspartic acid necessary for phosphatase activity. (**C**) Immunodetection of PPM-1.D::HA (yellow) and SUN-1 (magenta) in the progenitor zone (top) and at diplonema (middle) and diakinesis (bottom). Scale bars, 5 μm. (**D**) Dissected gonads stained for DAPI (top) and PPM-1.D::HA (bottom) in the wild type (left) and *prom-1* mutant (right). Scale bar, 10 μm. (**E**) Left: Western blot of trichloroacetic acid (TCA)–precipitated proteins from yeast expressing PPM-1.D::LexA, PROM-1::HA in the absence or presence of the proteasome inhibitor, MG132. For full photographs of the blots, see fig. S5A. Right: Quantification of PPM-1.D::LexA in Western blots (*n* = 2) normalized to the level of PPM-1.D::LexA when both PROM-1 and PPM-1.D are expressed.

amount of chromatin-bound PPM1D/WIP1-ATM complex regulates the duration of cell cycle arrest after DNA damage induction (*27*).

C. elegans PPM-1.D has a phosphatase type 2C domain (PP2C; Fig. 2B), which classifies it as a member of the PP2C family (*28*). The *jf76* allele, which suppresses the high level of embryonic death seen in the *prom-1* mutant, bears a G-to-C transversion that abolishes splicing and leads to a premature stop codon. This causes loss of the last two exons, similar to the *tm8369* allele (Fig. 2B). Notably, these truncation alleles still carry the well-conserved PP2C domain (Fig. 2B). Therefore, we also generated a null deletion allele of *ppm-1.D* (*jf120*) (Fig. 2B). We validated this allele as null by quantitative reverse transcription polymerase chain reaction (qRT-PCR; fig. S3A). Both the truncation and null alleles displayed a small increase in embryonic lethality originating from both defective oogenesis and spermatogenesis (fig. S3, B and C). At very low frequency (means ± SD, 2.6 ± 1.0%; *n* = 1914), homozygous null *ppm-1.D* mutants sired progeny with abnormal body morphology, indicating developmental defects (fig. S3D).

Immunodetection of the tagged PPM-1.D (see table S1 for functionality of the tagged lined) revealed a strong nuclear signal throughout the progenitor zone, which disappeared as soon as cells entered meiosis (Fig. 2C, top). The nuclear signal displayed a marked intensity increase at the nuclear periphery. In the proximal germ line, the PPM-1.D signal reappeared in diplonema as foci (Fig. 2C, middle), and later, a strong nuclear signal with enrichment at the nuclear periphery could be seen at diakinesis (Fig. 2C, bottom). The human ortholog PPM1D is reported to be expressed in response to p53 induction (*29*). C. Elegans P-53-like protein-1 (CEP-1) (worm p53) is coexpressed in the germline progenitor zone [e.g., (*30*)]; therefore, we examined tagged PPM-1.D in the *cep-1* mutant (fig. S4). PPM-1.D expression was independent of *cep-1* in the germ line. To test whether PPM-1.D is a substrate of the SCF^{PROM-1} ubiquitin ligase for targeted protein degradation, we examined the localization of PPM-1.D in the *prom-1(ok1140)* deletion background. In the *prom-1(ok1140)* mutant, PPM-1.D failed to disappear at meiotic entry and was detected at all stages of meiotic prophase (Fig. 2D), suggesting scheduled degradation of PPM-1.D by SCF^{PROM-1}.

To test whether PPM-1.D is a direct PROM-1 substrate, we took advantage of the yeast *Saccharomyces cerevisiae*, which contains the conserved SCF complex subunits but lacks a PROM-1 homolog. When PPM-1.D or PROM-1 was individually expressed in yeast, each protein was readily detected by Western blotting. However, as soon as PROM-1 and PPM-1.D were coexpressed, PPM-1.D levels were significantly reduced (Fig. 2E, left, and fig. S5A). Addition of the proteasome inhibitor MG132 to cells coexpressing PROM-1 and PPM-1.D led to a sixfold increase in PPM-1.D levels (Fig. 2E, right), reinforcing the hypothesis that the observed reduction of PPM-1.D is due to PROM-1–mediated degradation. This finding supports the idea that PPM-1.D is a target of the SCF^{PROM-1} complex.

PPM-1.D is a conserved protein with a well-known role in the response to DNA damage in mammals (*31*). Here, we identify a previously unknown activity at the stage of meiotic entry, when meiotic progenitor cells differentiate. PPM-1.D has to be degraded by SCF^{PROM-1} to mediate scheduled meiotic entry.

CHK-2 and PPM-1.D are found together in protein complexes
As deleting *ppm-1.D* significantly rescues the meiotic *prom-1* mutant phenotypes and PPM-1.D is mostly expressed in the progenitor zone, we used endogenously tagged *ha::ppm-1.*D to determine the

PPM-1.D interactome. Biochemical fractionation of germline cells revealed that PPM-1.D was enriched in the soluble and insoluble nuclear fractions (Fig. 3A and fig. S5B). This is in agreement with our cytological analysis that PPM-1.D is detected in the nucleoplasm and enriched at the nuclear rim (Fig. 2C).

Next, triplicate immunoprecipitation experiments of HA::PPM-1.D from the pooled nuclear fractions followed by mass spectrometry analysis reproducibly identified CHK-2 as an interactor (Table 1, fig. S6A, and table S2). CHK-2 is a key meiotic regulator involved in controlling numerous prophase I events in *C. elegans* (*9*). To confirm the top-listed PPM-1.D–CHK-2 interaction, we tagged endogenous CHK-2 with an HA tag at the C terminus (see table S1 for functionality) and performed triplicate immunoprecipitation experiments, followed by mass spectrometry analysis. PPM-1.D was consistently found in protein complexes containing CHK-2 kinase as top hit (Table 1, fig. S6B, and table S3).

PPM-1.D and CHK-2 reside inside the nucleus
Since PPM-1.D and CHK-2 were reciprocally found as prime interactors in coimmunoprecipitations, we asked whether PPM-1.D and CHK-2 would also reside in the same subcellular compartments in vivo (comprehensive CHK-2 localization in the germ line has not been reported to date). We generated a strain expressing both HA::PPM-1.D and CHK-2::3×FLAG (for functionality of the CHK-2::3×FLAG, see table S1) and examined their colocalization using stimulated emission depletion (STED) microscopy. In the progenitor zone, PPM-1.D and CHK-2 showed notable colocalization in the nucleus, where both proteins were enriched at the nuclear periphery (Fig. 3B) and showed a high degree of staining overlap [automatic threshold Manders coefficient (means ± SD): CHK-2 = 0.86 ± 0.06 and PPM-1.D = 0.89 ± 0.05; four nuclei each].

To assess whether CHK-2 enriched at the nuclear rim was inside or outside the nuclear membrane, we used electron microscopy with immunogold labeling. After validating the specificity of the antibody (fig. S7), we focused on the nucleopores. In cryosections from progenitor zone nuclei, CHK-2 was in close vicinity to the nucleopore in 38% of cases (13 of 34 nucleopores; Fig. 3C). At this resolution, CHK-2 was found highly enriched in the nucleus both at the nuclear rim and inside the nucleus, and a smaller fraction was detected in the cytoplasm (Fig. 3D). To quantify the signal, we divided each nucleus into three zones of equal area (Fig. 3E, zones 1 to 3) and added a fourth zone (zone 0) that is equidistant from the nuclear membrane as zone 1 and represents the vicinity just outside of the nucleus. In each zone, we counted the number of gold particles detected in progenitor zone nuclei (Fig. 3F; *n* = 20 nuclei). CHK-2 was mostly nuclear: 84.1 ± 9.6% of the gold particles were inside the nucleus and enriched in zone 1 (41.3 ± 6.2%), just interior to the nuclear membrane. We conclude that in germline progenitor zone nuclei, CHK-2 is located inside the nucleus and PPM-1.D and CHK-2 strongly colocalize at the nuclear periphery.

PPM-1.D directly interacts with CHK-2
As PPM-1.D and CHK-2 were found associated in protein complexes and share the same location inside the nucleus, we tested whether these *C. elegans* proteins interact directly. With this aim, we constructed Maltose-Binding Protein (MBP)–PPM-1.D–10×HIS and glutathione S-transferase (GST)–CHK-2–3×FLAG and expressed these proteins in *Escherichia coli*. Both proteins were expressed and detectable in cell lysates (Fig. 3G, input lanes, and fig. S5C for whole
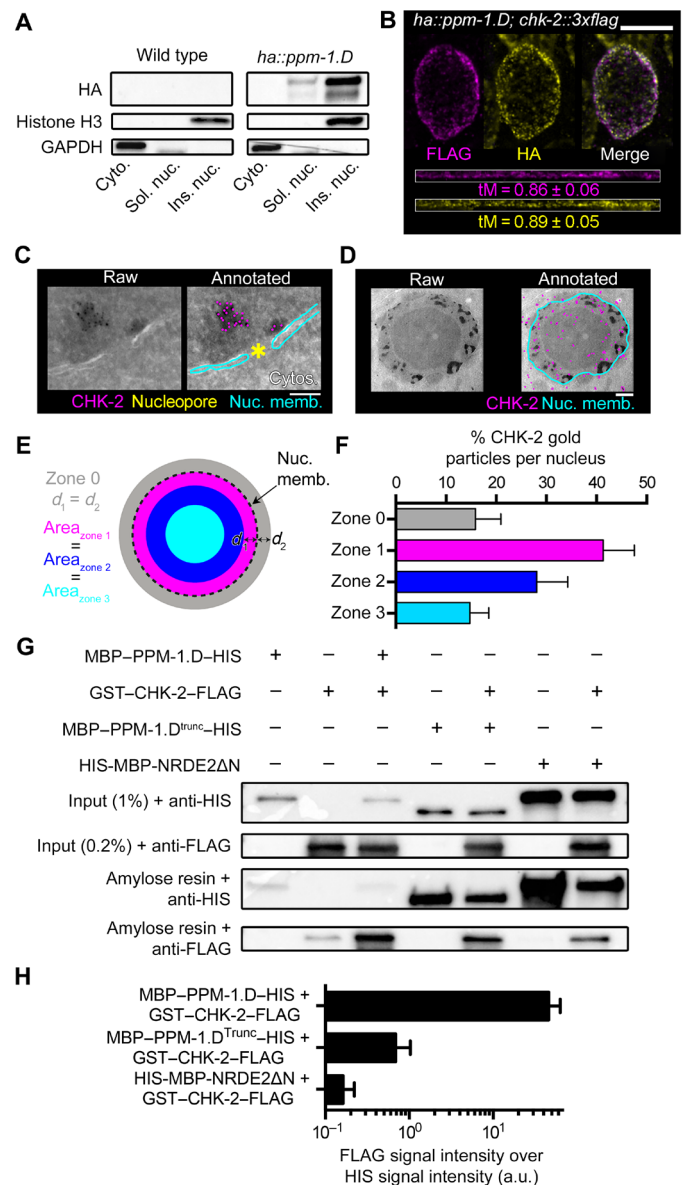
Fig. 3. PPM-1.D and CHK-2 colocalize in the progenitor zone and interact physically. (**A**) Western blot of cellular fractions (cytosolic, soluble nuclear, and insoluble nuclear) with the specified antibodies for the indicated genotypes. For full photographs of the blots, see fig. S5B. GAPDH, glyceraldehyde-3-phosphate dehydrogenase. (**B**) Stimulated emission depletion (STED)–visualized immunostaining of CHK-2::3×FLAG (magenta) and PPM-1.D::HA (yellow; top); straightened profiles of the signals (bottom). tM, automatic threshold Manders colocalization coefficient. Scale bar, 5 μm. (**C**) Left: Raw electron microscopy image of one nucleopore with gold particles indicating CHK-2. Right: With annotated nuclear membranes (cyan) and CHK-2 (magenta). Scale bar, 10 nm. (**D**) Left: Raw electron microscopy image of one mitotic nucleus with gold particles indicating CHK-2. Right: With annotated nuclear membranes (cyan) and CHK-2 (magenta). Scale bar, 100 nm. (**E**) Scheme used to divide the three nuclear zones of equal area (zones 1 to 3) and the outer vicinity of the nucleus (zone 0). (**F**) Distribution of CHK-2 gold particles in the four different zones. (**G**) Top: Western blot analysis after amylose purification of the indicated proteins expressed in *E. coli*. For full photographs of the blots, see fig. S5C. (**H**) Quantification of the FLAG signal (CHK-2) normalized to the HIS signal for the indicated colysed samples ($n = 2$ Western blots).

blots). Next, we subjected the cell lysates to pull-down assays using amylose beads. Amylose beads purified MBP–PPM-1.D–10×HIS (Fig. 3G, first lane, amylose resin + anti-HIS), with GST–CHK-2–3×FLAG displaying weak nonspecific binding to the beads (Fig. 3G, second lane, amylose resin + anti-FLAG). When independent cultures of MBP–PPM-1.D–10×HIS and GST–CHK-2–3×FLAG were lysed together and subjected to pull-down assays, MBP–PPM-1.D–10×HIS reproducibly copurified GST–CHK-2–3×FLAG (Fig. 3G, third lane, amylose resin + anti-FLAG), which suggests that PPM-1.D and CHK-2 can directly interact.

Next, we examined binding of the truncated PPM-1.D protein lacking the last two exons [corresponding to the (*tm8369* or *jf76*) alleles, further referred to as PPM-1.D^{trunc}; Fig. 2B]. Truncated PPM-1.D appeared more stable, was expressed more strongly than the full-length protein in *E. coli* (Fig. 3G, fourth lane, input, anti-HIS), and was very efficiently purified using amylose beads (Fig. 3G, fourth lane, amylose resin + anti-HIS). When CHK-2 was colysed with truncated PPM-1.D, we could only pull down low levels of CHK-2 compared with normalized amounts of protein pulled down with full-length PPM-1.D [Fig. 3, G (fifth lane, amylose resin + anti-FLAG) and H].

We also tested nonspecific binding of CHK-2 protein to the MBP affinity tag. For this, we expressed the unrelated human protein NRDE2 [10×HIS–MBP-3C–Necessary For RNA Interference, Domain Containing (NRDE2)ΔN], which has a similar molecular weight to PPM-1.D. After validating that we could efficiently purify 10×HIS–MBP-3C–NRDE2ΔN (Fig. 3G, sixth lane, amylose resin + anti-HIS), we colysed bacteria expressing GST–CHK-2–3×FLAG or MBP-3C–NRDE2ΔN-10×HIS and performed MBP pull-down assays. We found that similar amounts of CHK-2 were coimmunoprecipitated with 10×HIS–MBP-3C–NRDE2ΔN and MBP-3C–PPM-1.D–truncated–10×HIS (Fig. 3G, fifth and seventh lane respectively, amylose resin + anti-FLAG). The finding that the truncated PPM-1.D and NRDE2 both coimmunoprecipitated similar amounts of CHK-2 suggests that CHK-2 has some affinity binding to the MBP affinity tag, rather than to the truncated PPM-1.D protein.

Quantification of coimmunoprecipitated CHK-2, normalized to input PPM-1.D, revealed that CHK-2 binds to full-length PPM-1.D ~70-fold more efficiently than to PPM-1.D lacking the C terminus (encoded by the two last exons; Fig. 3H, bottom, quantification derived from two biological replicates). However, despite the reduced level of binding, CHK-2 binding to PPM-1.D^{trunc} was still four times greater than that to the MBP affinity tag (Fig. 3H). We, thus, conclude that the PPM-1.D C terminus is necessary for efficient interaction with CHK-2, either through direct binding or indirectly via allowing correct protein folding.

Furthermore, we tested whether the C-terminal domain of PPM-1.D (amino acids 568 to 766) could pull down CHK-2 in a similar assay (fig. S8A). PPM-1.D(568-766) binds 10 times less efficiently to CHK-2 compared with PPM-1.D (fig. S8B) but seven times more efficiently than PPM-1.D^{trunc} (fig. S8C). These results support the view that the PPM-1.D C terminus is required for interaction with CHK-2.

We note that CHK-2 displays unspecific background binding. However, the results of the coprecipitation experiments were comparable over several biological replicates, and quantification shows that significantly more CHK-2 binds to PPM-1.D than PPM-1.D lacking the C terminus or to the control protein NRDE2. Moreover, the isolated PPM-1.D C terminus also shows more binding to CHK-2

Table 1. Mass spectrometry results from HA pull-down assays. Peptide spectrum matches (PSMs) for the bait and control indicate how often peptides of a given protein were identified in each biological replicate. The log$_2$ ratios and P values are based on normalized summed peptide intensities, and statistical analysis was performed using LIMMA, with adjusted P values corrected for multiple testing (Benjamini-Hochberg procedure).

Bait	Hit	Unique peptides	Bait PSMs			Control PSMs			Log$_2$ ratio bait/control	P value	Adj. P value
			R1	R2	R3	R1	R2	R3			
HA::PPM-1.D	CHK-2	16	8	7	15	0	0	0	6.58	1.69×10^{-06}	7.04×10^{-04}
CHK-2::HA	PPM-1.D	29	13	24	48	0	0	0	6.20	3.96×10^{-05}	2.11×10^{-02}

than the controls. We are thus confident that CHK-2 and PPM-1.D interact directly, which is additionally supported by the mass spectrometry analysis. However, we cannot conclude on the stoichiometry and stability of the PPM-1.D–CHK-2 interaction, as this would require a deeper biochemical or biophysical characterization.

PPM-1.D restricts CHK-2 localization to the nuclear periphery

We first examined the pattern of CHK-2 and PPM-1.D localization in the progenitor zone, when germ cells enter meiosis. CHK-2 is expressed in the progenitor zone, overlapping with PPM-1.D (Fig. 3B). At the subcellular level, CHK-2 shows strong costaining with PPM-1.D at the nuclear rim in the progenitor zone. In contrast, at and after meiotic entry, enrichment at the nuclear rim is lost, and CHK-2 is mostly nucleoplasmic and localized to spots at the nuclear periphery (Fig. 4A), where it presumably colocalizes with putative substrates [e.g., pairing center proteins (14) or SUN-1 aggregates]. We next examined CHK-2 localization in *ppm-1.D(jf120)* null and in the C-terminal truncation mutant *ppm-1.D (tm8369)*, which does not interact with CHK-2; both alleles efficiently suppress the *prom-1(ok1140)* null phenotype (Fig. 4A and fig. S9). In both *ppm-1.D* mutant alleles, CHK-2 lost its nuclear rim enrichment in the progenitor zone, and only nucleoplasmic signal was visible (Fig. 4A). These results are consistent with a model in which PPM-1.D promotes the localization of inactive CHK-2 to the nuclear rim in progenitor zone cells; when PROM-1 degrades PPM-1.D at meiotic entry, CHK-2 becomes nucleoplasmic and active. Furthermore, as *ppm-1.D(tm8369)* results in loss of CHK-2 enrichment at the nuclear rim, we conclude that the C-terminal protein tail of PPM-1.D is necessary for CHK-2 enrichment at the nuclear rim in the progenitor zone.

We then asked whether the catalytic activity of the PPM-1.D phosphatase is involved in the localization of both PPM-1.D and CHK-2 to the nuclear rim. We mutated the aspartic acid (D) residue at position 274 to alanine to generate catalytically inactive PPM-1.D. D274 is highly conserved and is located in the PP2C domain (Fig. 4A); the exchange of aspartic acid to alanine in human PPM1D was previously shown to abolish phosphatase catalytic activity (32). *ppm-1.D(jf182* [PPM-1.D(D274A)]*)* was confirmed as genetically inactive PPM-1.D (fig. S10) since addition of hydroxyurea resulted in equal levels of dead embryos, as seen with the *ppm-1.D(jf120)* null allele. We also confirmed that abolition of the catalytic activity of PPM-1.D had no impact on its localization or stability (fig. S11). We next investigated the localization of CHK-2 in this mutant. Since CHK-2 nuclear rim staining was unaffected in *ppm-1.D(jf182[PPM-1.D(D274A)])*, we conclude that PPM-1.D catalytic activity is not required for nuclear rim enrichment of CHK-2 in the progenitor zone. This catalytically inactive allele of *ppm-1.D* failed to rescue the *prom-1* phenotype (Fig. 4A).

We also explored whether PPM-1.D localization to the nuclear periphery is dependent on CHK-2. Inactivation of *chk-2* with the *me64* allele, deletion of the previously identified paralogous gene, T08D2.7 [corresponding to *chkr-2(ok431)*] (9), or both mutations combined did not affect PPM-1.D nuclear rim staining (fig. S12). Therefore, we concluded that PPM-1.D enrichment at the nuclear periphery is *chk-2* and *chkr-2* independent. In summary, the sequestration of CHK-2 at the nuclear rim by PPM-1.D is independent of PPM-1.D phosphatase activity, and CHK-2 activation does not require PPM-1.D phosphatase activity. Loss of PPM-1.D, via SCF^{PROM-1}–mediated degradation, appears sufficient to liberate CHK-2 from the nuclear rim and allows the kinase to become active and initiate meiosis.

PPM-1.D levels are regulating CHK-2

As the truncated allele of *ppm-1.D*, *tm8369*, retains the PP2C domain, we tagged the truncated protein to assess its expression. Truncated PPM-1.D displayed reduced nuclear staining without marked nuclear periphery enrichment, in contrast to the bright nuclear rim staining of wild-type PPM-1.D (Fig. 4B). This reinforces the idea that the C-terminal part of PPM-1.D is necessary for enrichment at the nuclear periphery. Line profile analysis of the HA signal in *ha::ppm-1.D–truncated* worms across the nucleus showed that the detected signal is above the background level of antibody measured in untagged worms (Fig. 4B, right). We then compared mRNA levels of full-length and truncated *ppm-1.D*; this revealed that mRNA of the truncated allele *ppm-1.D(tm8369)* is expressed at wild-type levels (Fig. 4C, left). We also quantified the levels of both wild-type and truncated HA::PPM-1.D by Western blotting (Fig. 4C, center, and fig. S5D), normalized to histone H3. The level of truncated PPM-1.D protein was reduced by threefold compared with wild-type protein (Fig. 4C, right). We, therefore, conclude that the C-terminal part of PPM-1.D is necessary for protein stability. Moreover, we found that protein levels of both PPM-1.D and truncated PPM-1.D depend on SCF^{PROM-1} (fig. S13).

The loss of CHK-2 nuclear rim enrichment in the truncated allele (*tm8369*) could be due to either a reduction of PPM-1.D levels or the lack of the C-terminal part of PPM-1.D [which is required for in vivo interaction with CHK-2, as suggested in Fig. 3 (G and H)]. To resolve the issue, we silenced the cytoplasmic nucleopore protein Nuclear Pore complex Protein-9 (NPP-9) by RNA interference (RNAi) to reduce the levels of PPM-1.D in the nucleus. Conditional knockdown of the nuclear pore gene *npp-9* led to a threefold reduction in PPM-1.D staining in the wild type, both in the nucleus and at the nuclear rim (Fig. 4D, left). Moreover, silencing of *npp-9* reproducibly rescued the *prom-1* mutant phenotype (Fig. 4D, right). In *prom-1* mutants, the leptotene-zygotene–like zone extends, on average, for 45 ± 3 ($n = 6$) cell rows from the distal tip of the germ
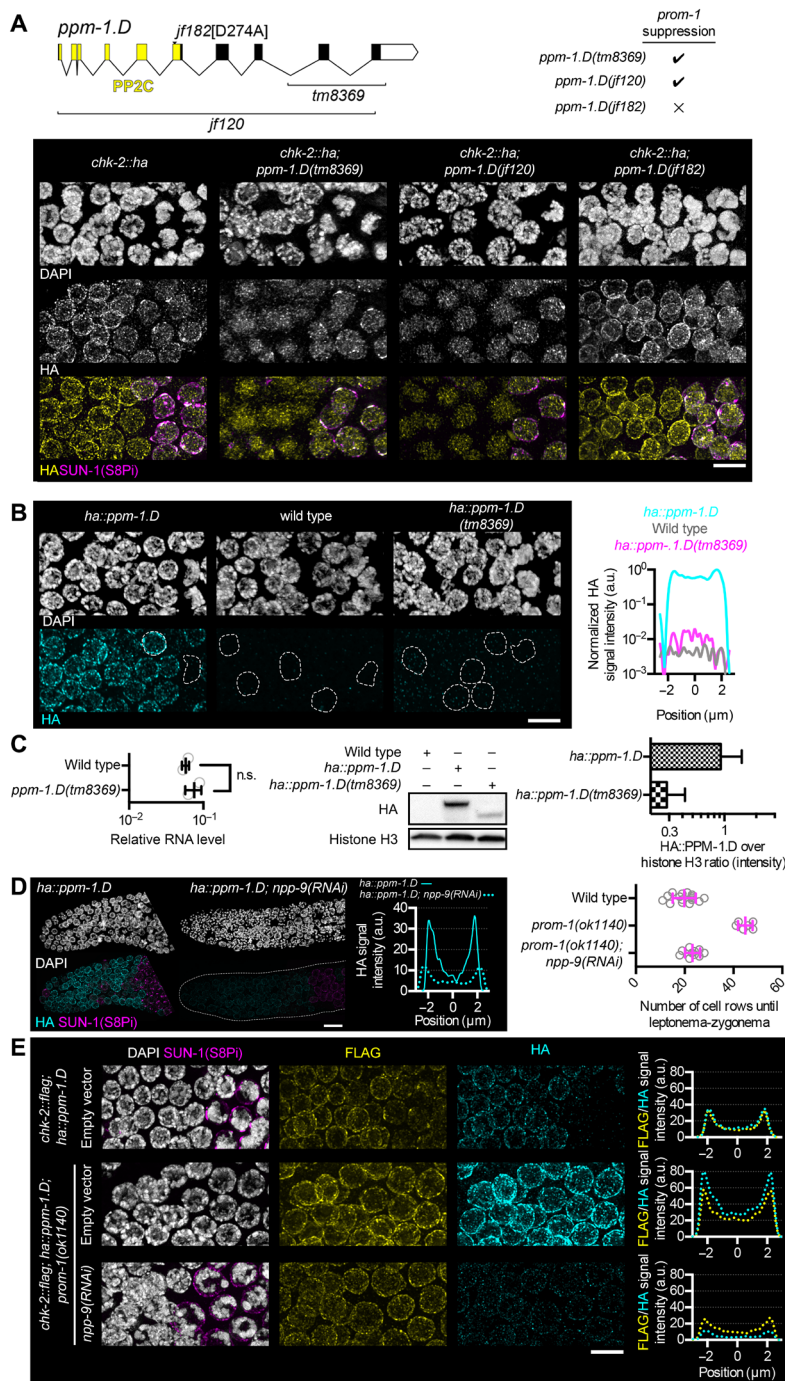
Fig. 4. Regulation of CHK-2 localization and activity by PPM-1.D. (**A**) Gene structure of *ppm-1.D*, showing the domain and exon/intron structure and alleles (top left), and genotypes suppressing the *prom-1* phenotype. DAPI staining (white) and HA immunostaining (yellow) in the progenitor zone for the indicated genotypes. The *jf182*[D274A] allele encodes catalytically inactive PPM-1.D. Scale bar, 5 μm. (**B**) Left: DAPI staining and HA immunodetection (cyan) in the progenitor zone for the indicated genotypes. Scale bar, 5 μm. Right: Average line profile analysis of HA signal intensity centered on the nucleus for the indicated genotypes (*n* = 25 nuclei from the progenitor zone). (**C**) Left: RNA quantification for *ppm-1.D* for the indicated genotypes. Data for the wild type are the same as in fig. S3A. Center: Western blot analysis of HA and histone H3 in whole-worm extracts for the indicated genotypes. For full photographs of the blots, see fig. S5D. Right: Quantification of the ratio of the HA signal intensity to histone H3 signal intensity for the indicated genotypes. n.s., not significant. (**D**) Left: DAPI staining and immunostaining of PPM-1.D::HA (cyan) and SUN-1(S8Pi) (magenta) in the distal tip for the indicated genotypes, showing the average line profile analysis of HA signal intensity centered on the nucleus for the indicated genotypes (*n* = 25 nuclei from the mitotic zone). Right: Number of cell rows before entry into meiotic prophase for the indicated genotypes. Scale bar, 10 μm. (**E**) DAPI staining and immunodetection of SUN-1(S8Pi) (magenta), FLAG (yellow), and HA (cyan) at transition from the progenitor zone to entry into leptonema-zygonema (at around 20 cell rows from the distal tip cell) for the indicated genotypes. Scale bar, 5 μm. Right: Average line profile analysis of HA signal intensity centered on the nucleus for the indicated genotypes (*n* = 25 nuclei from the mitotic zone).

line, whereas in *prom-1; npp-9 RNAi*, it extends for 23 ± 3 (*n* = 10) cell rows, which is similar to that in the wild type (20 ± 5 cell rows, *n* = 16).

We next examined PPM-1.D and CHK-2 localization in the *prom-1* mutant with and without *npp-9(RNAi)* to further investigate the mechanism responsible for rescue of the phenotype. After *npp-9(RNAi)* treatment, PPM-1.D levels were reduced by threefold compared with wild-type levels (Fig. 4E, right) and at least seven times compared with *prom-1* levels. This threefold reduction is sufficient to promote scheduled meiotic entry, as demonstrated by the timely phosphorylation of the CHK-2 substrate SUN-1 serine-8 SUN-1(S8Pi) (*10*). In addition, CHK-2 was both localized to the nuclear interior and associated with the nuclear rim. We conclude that (i) enrichment of CHK-2 to the nuclear rim is mediated by the C-terminal part of PPM-1.D and (ii) CHK-2 activity is responsive to the levels of PPM-1.D. Together, these data indicate that the C-terminal part of PPM-1.D is necessary for localization of CHK-2 to the nuclear rim and that C-terminal truncation of PPM-1.D leads to protein instability. In addition, the level of PPM-1.D regulates CHK-2 activity.

Loss of PPM-1.D–mediated CHK-2 inhibition leads to premature meiotic entry

PPM-1.D inhibits CHK-2; to promote meiotic entry, PPM-1.D is actively removed by SCF^PROM-1–mediated proteolysis, leading to activation of CHK-2, which is strongly correlated with relocation from the nuclear periphery to the nuclear interior. To test whether loss of PPM-1.D leads to premature meiotic entry, we costained for CYE-1, a cyclin whose distal germline accumulation is restricted to the progenitor cell zone via SCF^PROM-1–mediated proteolysis at meiotic entry (*33*, *34*), and SUN-1(S8Pi), a meiotic prophase marker for CHK-2 activity (Fig. 5A, top) (*10*). These two markers show largely mutually exclusive accumulation: Nuclei expressing both markers were only rarely observed in the wild type (Fig. 5A). Notably, in the *ppm-1.D* null allele, we found a consistent overlap of CYE-1 and SUN-1(S8Pi) accumulation in all germ lines analyzed (Fig. 5A, bottom). We interpret this finding as indicating that the appearance of SUN-1(S8Pi) before down-regulation of CYE-1 is caused by premature activation of CHK-2.

We next examined protein staining in the *ppm-1.D* C-terminal truncation mutant, *tm8369*, and also found significant overlap of CYE-1 and SUN-1(S8Pi) accumulation, although the extent of overlap was smaller than with the *ppm-1.D* null allele. On the basis of this difference, we hypothesize that both the catalytic activity and the C-terminal domain of PPM-1.D contribute to CHK-2 inhibition and prevention of premature meiotic entry. To test this hypothesis, we mutated aspartic acid 274 (which leads to loss of catalytic activity) in the truncated *ppm-1.D* allele (intragenic double mutant *jf181*) and observed a significant increase in overlap between the two markers compared with the wild type and the C-terminal truncation mutant (Fig. 5A, bottom). In contrast, removing only the catalytic activity of PPM-1.D did not lead to overlap between the markers. These results are in agreement with our previous observation that inactivation of the PPM-1.D catalytic domain alone is insufficient to rescue the meiotic defects of *prom-1*. We propose that PPM-1.D exerts control over meiotic entry at two levels: (i) by restricting CHK-2 localization to the nuclear periphery and (ii) by dephosphorylation of CHK-2 target proteins.

We next asked: What is the relationship between premeiotic S phase and meiotic entry in the *ppm-1.D* null mutant? To address this, we monitored DNA synthesis by 5-ethynyl-2′-deoxyuridine (EdU) incorporation into chromosomes (*35*). In the wild type, after 30-min pulse labeling, EdU incorporation and SUN-1(S8Pi) staining are mutually exclusive. Significantly, in the *ppm-1.D(jf120)* mutant, some cells entered meiosis [SUN-1(S8Pi)–positive cells] despite ongoing replication (EdU-positive cells; Fig. 5B). This phenotype was exclusively observed in the *ppm-1.D* null allele. To ensure that this result did not reflect a faster premeiotic S phase and meiotic entry or an accelerated rate of nuclear movement inside the gonad, we examined the size of the progenitor zone and mitotic markers in the *ppm-1.D(jf120)* mutant compared with the wild type. In addition, we inspected meiotic output and meiotic progression (table S4 and fig. S14). In each of these assays, the *ppm-1.D(jf120)* mutant behaved like the wild type.

As our results suggested that in the absence of PPM-1.D, CHK-2 is prematurely activated, we looked for possible direct consequences that could arise from premature CHK-2–induced meiotic entry. We reasoned that premature activation of CHK-2 might lead to uncoupling between meiotic chromosome axis formation [marked by High Incidence of Males-3 (HIM-3) loading (*36*)] and SUN-1(S8Pi). HIM-3 loading is independent of CHK-2, in contrast to SUN-1 phospho-modification (*18*). SUN-1(S8Pi)–positive nuclei were observed in which HIM-3 had not assembled onto the chromosome axes; this is never the case in the wild type (Fig. 5C, left). The degree of uncoupling between HIM-3 loading and SUN-1(S8Pi) was more prominent and significant in the *ppm-1.D* null allele (Fig. 5C, right).

To confirm that lack of PPM-1.D is sufficient to activate CHK-2, we took advantage of the *gld-1(q485) gld-2(q497)* double mutant, which produces largely tumorous germ lines in which only very few cells enter meiosis; these cells eventually revert to the progenitor fate (*2*). The few apparently meiotic cells were devoid of PPM-1.D but showed HIM-3 expression and CHK-2–mediated phosphorylation of pairing center proteins (Fig. 5D, High Incidence of Males-8 (pHIM-8)/Zinc finger In Meiosis (ZIMs) (*14*). Briefly, 33.2 ± 10 of the "meiotic nuclei" were positive for both HIM-3 and pHIM-8/ZIMs, and among those, 95% were negative for PPM-1.D (*n* = 5 gonads). We conclude that the progenitor fate is associated with the presence of PPM-1.D and that loss of PPM-1.D correlates well with the presence of active CHK-2.

We also examined the kinetics of chromosome alignment and pairing in the *ppm-1.D* mutants by fluorescence in situ hybridization (FISH) analysis using a probe for the *5S* ribosomal RNA gene cluster. Chromosome pairing was delayed in both *ppm-1.D jf120* and *tm8369* compared with the wild type (Fig. 5E); however, by pachynema, the extent of pairing in these mutants was indistinguishable from the wild type. Both *ppm-1.D* mutant alleles accumulated higher amounts of the marker of the meiotic recombination, RAD-51 (*37*, *38*), as well as delayed clearance during the meiotic time course, which indicates that recombination is impeded. Nonetheless, RAD-51 foci disappeared, which suggests successful repair (Fig. 5F and table S5). In summary, we propose that meiotic entry in the wild type follows the completion of meiotic S phase and that premature meiotic entry interferes with the kinetics of chromosome pairing and meiotic recombination. Furthermore, we propose that both catalytic and noncatalytic activities of PPM-1.D work together to prevent premature meiotic entry.

PPM-1.D involvement in the DNA damage response is conserved

Reminiscent to the role of mammalian PPM1D/Wip1 in the DNA damage response (*26*), we found that *ppm-1.D* mutants are
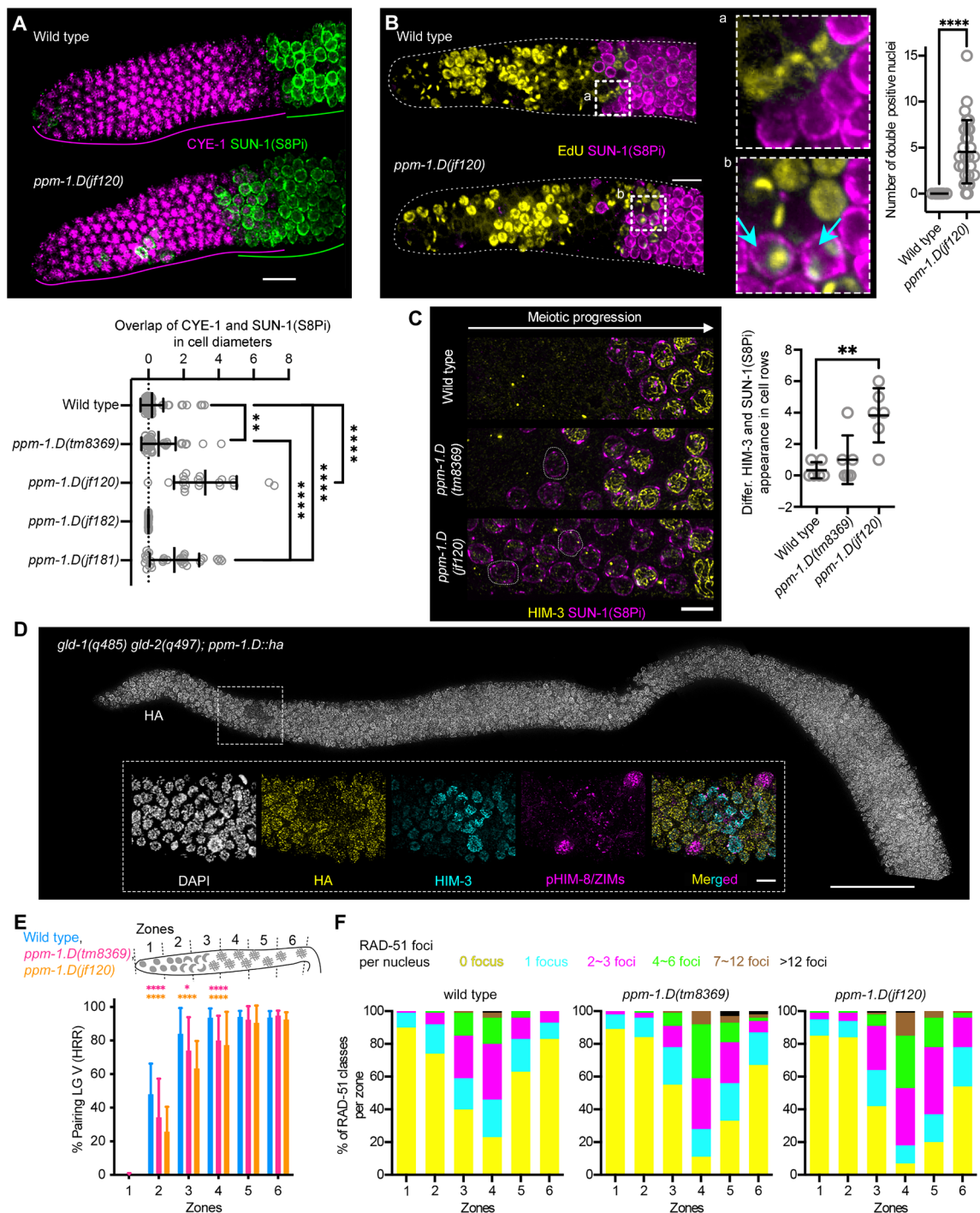
Fig. 5. Premature meiotic entry in *ppm-1.D* mutants. (**A**) Top: Immunostaining of CYE-1 (magenta) and SUN-1(S8Pi) (green) in the progenitor zone for the indicated genotypes. Scale bar, 10 μm. Bottom: Distribution of the overlap between CYE-1 and SUN-1(S8Pi) staining in cell diameters, for the genotypes shown. **$P < 0.01$ and ****$P < 0.0001$ for the Mann-Whitney test. (**B**) Left: EdU incorporation into replicating DNA (yellow) and SUN-1(S8Pi) staining (magenta) for the indicated genotypes. Blue arrows in the inset highlight nuclei with both significant EdU incorporation (indicating ongoing meiotic S phase) and SUN-1(S8Pi) staining (indicating CHK-2 activity and meiotic entry). Scale bar, 10 μm. Right: Quantification of double-positive nuclei for the indicated genotypes. ****$P < 0.0001$ for the Mann-Whitney test. (**C**) Left: DAPI staining and immunostaining of HIM-3 (yellow) and SUN-1(S8Pi) (magenta). Scale bar, 5 μm. Right: The cell row number at which HIM-3 and SUN-1(S8Pi) appear in the germ line, for the indicated genotypes. Cell rows were counted as positive when more than half of the cells showed positive staining. **$P < 0.01$. (**D**) Top: Immunostaining of HA in *gld-1(q485) gld-2(q497); ppm-1.D::ha* mutant worms. Scale bar, 50 μm. Insets show a higher magnification for nuclei stained with DAPI (white) and for HA (yellow), HIM-3 (cyan), and pHIM-8/ZIMs (magenta) in the boxed zone in the top picture. Scale bar, 5 μm. (**E**) Dissected gonads were divided into six zones of equal length. The percentage of nuclei with a paired FISH signal (*5S* probes on chromosome V) in each zone for the indicated genotypes. *$P < 0.05$ and ****$P < 0.0001$ for the Fisher's exact test. (**F**) Percentage of nuclei with the specified numbers of RAD-51 foci in each zone for the indicated genotypes. *P* values for the Fisher's exact test are shown in table S5.

sensitive to replicative stress caused by hydroxyurea (fig. S10). We further reason that if PPM1D/Wip1 function is conserved in *C. elegans*, then mutants might display an increase of apoptosis in the germ line due to accumulating DNA damage. Whereas germline apoptosis in *C. elegans* is physiological (*39*), it can also be induced by a genome integrity checkpoint triggered by DNA damage (*40*). CEP-1, the p53 homolog, mediates apoptosis of germ cells with persistent DNA damage. We, therefore, quantified apoptosis in the *ppm-1.D* mutants using SYTO-12 as a reporter (*41*). The significantly increased apoptosis was *cep-1*/p53 dependent in both *ppm-1.D* truncation (*tm8369*) and null (*jf120*) alleles and largely independent of the meiotic DNA DSBs induced by the topoisomerase-like enzyme homolog of yeast SPOrulation gene-11 (SPO-11) (*40*) (Fig. 6 and table S6). We therefore concluded that *ppm-1.D* mutants accumulate unrepaired DNA lesions.

DISCUSSION

PPM-1.D is a PP2C phosphatase, and we isolated a recessive loss of function *ppm-1.D* allele in a screen aimed at suppressing the meiotic entry defects in the *prom-1* mutant. We found that, similar to the mammalian protein (*31*), PPM-1.D has a well-established canonical role in the DNA damage response. We identified a previously unknown function for PPM-1.D as a prominent factor involved in the transition from progenitor cell fate to differentiation at meiotic entry. PPM-1.D is expressed in germline progenitor zone cells, and our data suggest that it is actively degraded by SCF^PROM-1 at meiotic entry; it seems to be a major target of SCF^PROM-1, as evidenced by the restoration of high levels of embryonic viability upon suppression of
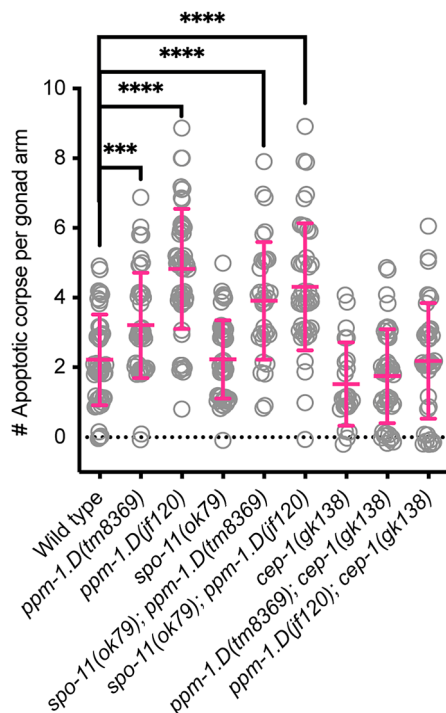
Fig. 6. PPM-1.D functions in the DNA damage response. Quantification of apoptotic corpses (scatter and means ± SD) for the indicated genotypes. ***$P < 0.001$ and ****$P < 0.0001$ for the Mann-Whitney test. Diagonal matrix with P values for Mann-Whitney test for all genotypes is in table S6.

prom-1 defects. Our mass spectrometry data identified CHK-2 as the main interacting partner of PPM-1.D, and we showed that the two proteins interact through the C-terminal domain of PPM-1.D. Moreover, we found that the C-terminal domain of PPM-1.D sequesters CHK-2 at the nuclear rim, thereby promoting CHK-2 inactivation. Premature meiotic entry in *ppm-1.D* mutants leads to low levels of embryonic death, elevated rates of apoptosis, meiotic entry before completion of meiotic S phase, the uncoupling of certain meiotic events (e.g., meiotic chromosome axis formation and chromosome end mobilization), and delayed chromosome pairing, which are associated with altered kinetics of meiotic recombination. *ppm-1.D* hermaphrodites sire progeny with developmental defects at a low rate, which could be explained by erroneous DNA repair taking place with a defective DNA damage response.

Control of meiotic entry in *C. elegans*

We propose the following model for meiotic entry in *C. elegans* (Fig. 7). In the progenitor zone germ cells, PPM-1.D enters the nucleus, where it directly interacts with CHK-2 and sequesters CHK-2 to the nuclear periphery. Sequestration of CHK-2 depends on the C-terminal part of PPM-1.D protein and does not require its phosphatase activity. Colocalization at the nuclear rim represents the first layer of control of PPM-1.D over CHK-2. When we engineered a *ppm-1.D* mutant lacking both the C terminus and the catalytic activity (leaving the rest of the protein intact), we found that premature meiotic entry was more pronounced than in the single mutants. We propose that both PPM-1.D–mediated sequestration and phosphatase activity inhibit CHK-2 in the progenitor zone, although sequestration may be the predominant inhibitory mechanism. Meiotic entry is initiated via the programmed degradation of PPM-1.D mediated by the SCF^PROM-1 complex. This leads to the release of CHK-2 from the nuclear periphery, which enables CHK-2 to drive important processes during meiosis. The CHK-2–antagonizing activity of PPM-1.D appears to be concentration dependent. The amount of nuclear PPM-1.D may act like a toggle switch for CHK-2 activity, as suggested by *npp-9* RNAi rescue of the *prom-1* mutant. Here, only the nuclear amount of PPM-1.D was decreased, but CHK-2 remained associated with the nuclear periphery to a certain extent; however, sufficient active CHK-2 was generated to rescue *prom-1*.

Dual function of PPM-1.D at meiotic entry

The PP2C phosphatase PPM-1.D first sequesters the meiotic key regulator CHK-2 (noncatalytic regulation), and then its phosphatase activity is involved in inactivating several relevant targets for meiotic entry (catalytic regulation), of which CHK-2 may be one. The function of enzymes is not always restricted to their catalytic activity. For example, mammalian histone modifiers also exhibit noncatalytic roles in noncanonical processes such as promoting cancer cell proliferation (*42*), suggesting that enzymes with both noncatalytic and catalytic roles may be more common than previously expected. Similarly, there is growing evidence that phosphatases can lose their catalytic activity and gain noncatalytic activities through evolution (*43*). Such pseudo-phosphatases are involved in processes ranging from competition for substrate binding to spatial anchoring of binding partners. In the outlined model of meiotic entry, PPM-1.D does not lose its phosphatase activity; instead, it exerts most of its control on CHK-2 via spatial sequestration of CHK-2 at the nuclear periphery, thereby preventing premature meiotic entry.
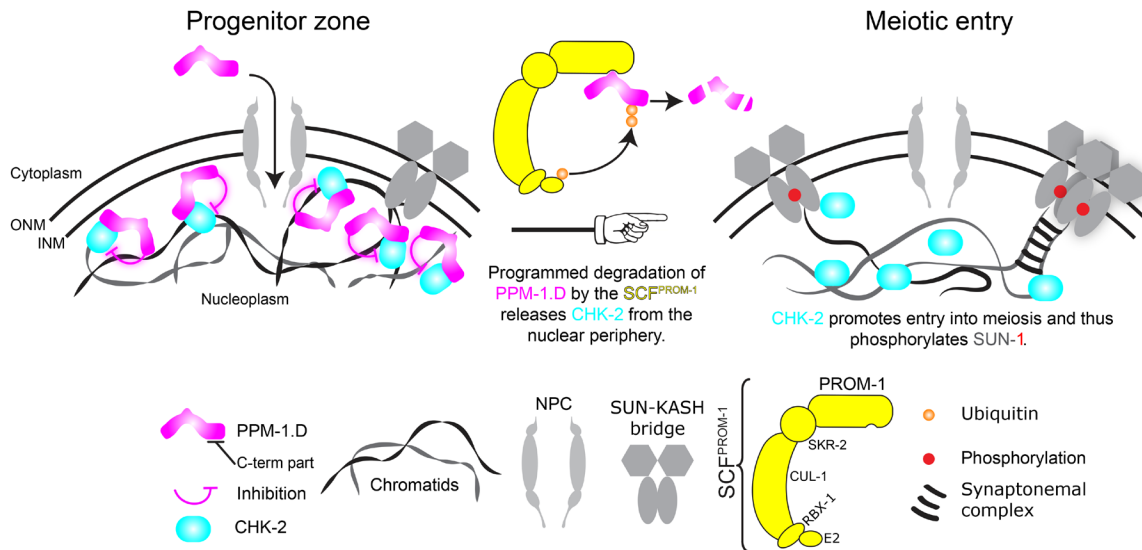
Fig. 7. Model of control of meiotic entry by PPM-1.D. Entry of PPM-1.D into the nucleus is mediated by nucleopores in the progenitor zone. Inside the nucleus, the C terminus of PPM-1.D interacts directly with CHK-2 and inhibits CHK-2 by both sequestering it at the nuclear periphery and dephosphorylation. At meiotic entry, SCF^PROM-1 degrades PPM-1.D. After the scheduled degradation of PPM-1.D, CHK-2 is released from the nuclear periphery and gains access to its substrates, thereby launching the initial events of meiotic prophase. C-term, C terminus; ONM, Outer nuclear membrane; INM, Inner nuclear membrane; NPC, Nucleo Pore Complex; SUN, Sad-1 and UNC-84; KASH, Klarsicht; ANC-1, SYNE homology.

Regulation of CHK-2 by PPM-1.D and other potential targets

CHK-2 appears to be negatively regulated by PPM-1.D; however, there may be additional layers of regulation of CHK-2 in the progenitor zone. In *ppm-1.D* mutants, inappropriate activation of CHK-2 [as indicated by the premature appearance of SUN-1(S8Pi)] is restricted to a couple of cell rows before meiotic entry and does not occur throughout the entire progenitor zone. This could mean either that CHK-2 activation is regulated independently of PPM-1.D in the more distal region of the progenitor zone or that CHK-2 requires an activation step in addition to loss of inhibition by PPM-1.D. Moreover, CHK-2 may not be the only target of the phosphatase PPM-1.D, since the *prom-1* phenotype is more severe than the *chk-2* phenotype. *prom-1* mutants display defective cohesion and chromosome axis protein loading, which is not evident in *chk-2* mutants. PROM-1 has also been shown to function in the degradation of mitotic cell cycle proteins at meiotic entry (*2*). It will be interesting to see, whether this function is mediated by PPM-1.D and whether PPM-1.D functions in the regulation of other meiotic proteins. Chromosome axis morphogenesis is not mediated by CHK-2 (*18*); thus, PPM-1.D might also regulate other DNA damage response kinases, such as the Ataxia Telangectasia mutated-Like-1 (ATL-1) kinase, at this important transition. Uncoupling of chromosome axes loading and SUN-1 phospho-modification was less prominent in the *tm8369* truncation allele, which retains the catalytic activity of PPM-1.D. This hints that chromosome axis morphogenesis may be predominantly under the control of the dephosphorylation activity of PPM-1.D.

Conservation of the DNA damage response

In mammals, PPM1D/Wip1 is involved in the DNA damage response and the apoptotic response (*26*), and the protein is often overexpressed in cancer (*44*). In *C. elegans*, PPM-1.D is also involved in the response to DNA damage. Since PPM-1.D is also detected in the embryos (Fig. 2D; see the embryo next to the progenitor zone tip), it would be very interesting to investigate its involvement in the regulation of the DNA damage response during developmental processes. Up-regulation of PPM1D/Wip1 expression in many human cancers makes the protein an attractive potential target for cancer therapy (*44*). It would be very interesting to determine whether the human homolog of PROM-1, F-Box Protein 47 (FBXO47), specifically degrades PPM1D/Wip1. Renal carcinoma samples have been identified with deletions in FBXO47 (*19*); thus, it would be highly interesting to find whether PPM1D/Wip1 also qualifies as a target for FBXO47 and whether germline tumors are associated with mutations in FBXO47 in humans.

MATERIALS AND METHODS

Nematode strains, strain construction, and culture conditions

All strains listed are derivatives of N2 Bristol (table S7) and were cultivated under normal conditions (*45*). CRISPR editing was done as previously described (*46*), except for *prom-1::ha*, which was generated using another published method (*47*). Guide and repair template and genotyping primers are listed in table S8, and plasmids used for *prom-1::ha* are listed in table S9.

Ethyl methane sulfonate screen

prom-1(ok1140) unc-55(e402) worms were grown on *E. coli*–seeded plates for 5 days. On day 6, the worms were collected in M9 buffer (0.3% KH_2PO_4, 0.6% Na_2HPO_4, 0.5% NaCl, and 1 mM $MgSO_4$) and washed three times in M9 buffer to remove the *E. coli*. Mutagenesis was carried out in 50 mM ethyl methane sulfonate (EMS; Sigma-Aldrich, catalog no. M0880-1G). After mutagenesis, worms were allowed to recover until day 10 and then were bleached to synchronize the population. Single L4 hermaphrodites were transferred to

small agarose plates seeded with *E. coli*. Viability of the mutagenized worms was assayed by looking for overcrowded plates at the second generation (F1+F2; fig. S2A).

Cytological preparation of gonads and immunostaining
Immunofluorescence was performed as previously described (*48*). L4 hermaphrodites were incubated at 20°C for 24 hours. Gonads were then dissected from young adults into 1× phosphate-buffered saline (PBS), fixed in 1% formaldehyde for 5 min at room temperature, and frozen in liquid nitrogen. After postfixation in ice-cold methanol, nonspecific binding sites were blocked by incubation in PBS containing 1% bovine serum albumin (BSA) for at least 1 hour. Antibodies were diluted in 1× PBST (1 × PBS containing 0.1 % Tween 20) and incubated overnight at 4°C (for primary antibodies) or 2 hours at room temperature (for secondary antibodies). After washes in PBST, samples were mounted in VECTASHIELD Antifade (Vector Laboratories Inc., Burlingame, CA) containing 4′6-diamidino-2-phenylindole (DAPI; 2 mg/ml).

For visualization of pHIM-8/ZIMs and HIM-3 (Fig. 5D), hermaphrodite germ lines were dissected from 24-hour post-L4 adults in egg buffer [25 mM Hepes (pH 7.4), 118 mM NaCl, 48 mM KCl, 2 mM EDTA, 5 mM EGTA, 0.1% Tween 20, and 15 mM NaN$_3$] and fixed in 1% formaldehyde for 1 min before freezing in liquid nitrogen. Dissected germ lines were further fixed in methanol at −20°C for 1 min and rehydrated with PBST. Samples were then blocked with blocking reagent (Roche, catalog no. 11096176001) for 1 hour and incubated with primary antibodies overnight at 4°C. Primary and secondary antibodies are listed in table S10.

RNA interference
RNAi was done as previously described (*49*). Briefly, a single colony from the *npp-9* clone and the empty vector [Ahringer collection (*50*)] were grown overnight at 37°C in 2× TY medium supplemented with ampicillin (100 μg/ml). The next day, cells were pelleted at 3000*g* for 15 min and resuspended in 2× TY, and 150 μl of the suspension was used to seed nematode growth medium (NGM) plates containing 1 M IPTG (isopropyl-β-D-thiogalactopyranoside) and ampicillin (100 ng/ml). Bacterial growth was allowed at 37°C overnight. Prepicked L4 were added to the plates and left at 20°C for 48 hours before analysis.

RNA extraction and qRT-PCR
Adult worms from three medium NGM plates were collected into M9 and allowed to sink in 1.5-ml Eppendorf tubes on ice. The supernatant was removed, 250 μl of TRIzol was added, and the suspension was transferred to another 1.5-ml Eppendorf tube containing 150 μl of acid-washed beads. Worms were disrupted using a FastPrep-24 5G instrument (MP Biomedicals) with three cycles (6.5 m/s, 15 s, and 10-min pause at 4°C). The mixture of disrupted worms was transferred into a new 1.5-ml Eppendorf tube. After the addition of 50 μl of chloroform, samples were vortexed for 30 s and left at room temperature for 5 min. Next, samples were centrifuged at 13,500*g* for 15 min at 4°C. The clear top layer was transferred into a fresh 1.5-ml Eppendorf tube, and nucleic acids were precipitated by the addition of 125 μl of isopropanol. Samples were then centrifuged at 13,500*g* for 10 min at 4°C. The pellet was washed with 500 μl of 70% ethanol and centrifuged at 18,500*g* for 5 min at 4°C. The pellet was air-dried and dissolved in 10 μl of ribonuclease-free water. After deoxyribonuclease treatment using a Promega kit

(catalog no. M6101) following the manufacturer's instruction, cDNA synthesis was done using SuperScript III (Invitrogen, catalog no. 18080051) with random hexamers, as described in the kit. For the qPCR master mix, 100 ng of total RNA was used with the SensiFAST SYBR No-ROX Kit (Bioline, catalog no. BIO-98005), and we used an Eppendorf RealPlex 2 Mastercycler to read the plate. Cycle Threshold (CT) measures were done in triplicate in the qPCR machine, and experiments were duplicated. *pmp-3* was used as the reference (*51*), and specific primers located in the 5′ and 3′ regions of *ppm-1.D* were used to assess the RNA level. Results were analyzed using the delta-delta CT method (*52*). Primers are listed in table S11.

Microscopy and evaluation
Three-dimensional (3D) stacks of images were taken using either a DeltaVision or a DeltaVision Ultra High Resolution microscope equipped with 100×/1.40 oil immersion objective lenses and a custom softWoRx software package. Images acquired with the DeltaVision where deconvolved using the softWoRx deconvolution algorithm. Maximum intensity projections of deconvolved images were generated using ImageJ after adjustments of the maximums and background subtraction using a rolling ball radius of 50 pixels. Where specified, images of gonads consist of multiple stitched images. This was necessary because of the size limitation of the field of view at high magnifications. Stitching of images to build up entire gonads was performed manually in Adobe Photoshop. Fluorescence levels of stitched images were adjusted to each other in Adobe Photoshop to correct for auto-adjustment settings of the microscope.

Superresolution images were acquired as single frame with an Abberior Instruments STEDYCON using an alpha Plan-Apochromat 100×/1.46 Oil DIC objective lens with two avalanche photodiode detectors for dual-channel 2D STED (orange and dark red), with samples prepared as previously described, except that samples were not mounted in DAPI but in Abberior mounting medium.

Fluorescence in situ hybridization
The FISH protocol was based on a published protocol (*53*). Dissected gonads were fixed in 4% paraformaldehyde in egg buffer for 2 min at room temperature and then stored in methanol at −20°C. Slides were then incubated in methanol at room temperature for 20 min, followed by 1-min washes in 50% methanol and 1× Saline Sodium Citrate buffer with 0.1% Tween-20 (SCCT) and dehydration by sequential immersion in 70, 90, and 100% ethanol (3 min each). Hybridization mixture containing 10.5 μl of FISH buffer (1 ml of 20× SCCT, 5 ml of formamide, 1 g of dextran sulfate, and 4 ml of H$_2$O) and 2.5 μl of labeled probe was added to air-dried slides. The FISH probe for the 5*S* ribosomal DNA (rDNA) locus (chromosome V) was made by labeling 1 μg of DNA with the DIG-Nick Translation Kit (Roche). After the addition of EDTA, the probe was incubated at 65°C for 10 min. PCR-amplified 5*S* rDNA was used to probe the right end of chromosome V and was labeled by PCR with digoxigenin-11–deoxyuridine triphosphate. Slides were incubated at 37°C overnight in a humidified chamber and then washed twice (20 min) at 37°C in the following buffer: 50% formamide, 2× SCCT, and 10% Tween 20. After three washes in 2× SCCT at room temperature, samples were blocked for 1 hour in 2× SCCT containing 1% BSA (w/v). Slides were then incubated in secondary anti-biotin antibody diluted in 2× SCCT (1:500) for 2 hours at room temperature, followed by three washes in 2× SCCT, then stained with DAPI (1 ng/ml), and mounted in VECTASHIELD.

Hydroxyurea treatment

Worms, 24 hours after L4 stage, were transferred to NGM plates containing 40 mM hydroxyurea seeded with *E. coli* for 8 hours. Worms were recovered and transferred to NGM plates seeded with *E. coli*. Each day, worms were transferred to fresh plates, and on day 3, embryonic viability of the laid eggs was assessed.

SYTO-12 staining

Young adults (24 hours after L4 stage) were soaked in 33 μM SYTO-12 (Thermo Fisher Scientific, catalog no. S7574) in PBS for 2 to 3 hours at 20°C in the dark, transferred to unseeded NGM plates for 30 to 60 min, and then mounted. SYTO-12–positive cells were scored within the germ line using an epifluorescence microscope equipped with a 40× or 63× oil immersion objective lens.

Imaging and quantification of PROM-1 levels

Immunostaining was carried out as previously described (*2*). Briefly, synchronized 24-hour post-L4 adult worms of the desired genotype were dissected in PBST containing 0.2 mM levamisole to extrude the gonads. The gonads were fixed in 3% paraformaldehyde for 10 min and then postfixed in chilled (−20°) methanol for 10 min. After washing three times for 10 min with PBST, they were blocked in 30% goat serum for 30 min at room temperature and then incubated with the desired primary antibodies diluted in 30% goat serum at 4° overnight. The next day, gonads were washed three times for 10 min in PBST and then incubated with appropriate secondary antibodies diluted in 30% goat serum at 4° overnight. After three 10-min washes with PBST, the gonads were incubated with DAPI (0.1 g/ml) in PBS for 30 min. After removal of excess liquid, the gonads were mixed with anti-fading agent (DABCO, 1,4-Diazabicyclo-[2,2,2-octan]) and transferred to an agarose pad on a slide.

Quantification of PROM-1::HA was based on a published method (*54*) with some modifications. Dissected gonads were stained with primary antibodies against the HA tag and against WAPL-1 and with DAPI. Hyperstack images were captured using a spinning disk confocal microscope (PerkinElmer-Cetus, Norwalk, CT). Exposure time for each channel was kept constant for each experiment. Two overlapping hyperstack images were captured to obtain a coverage of ~50 cell diameters from the distal end of the gonad. The images were further processed in Fiji, and DAPI staining of nuclei was used to mark cell diameters. Starting at the distal end, a cell-diameter profile (of intensity) was extracted for each gonad using a custom Python script and stored in text files. Intensity data were processed in R to visualize protein levels. Since PROM-1 quantification was carried out using antibodies against HA-tagged PROM-1, staining in N2 (which lacks HA-tagged PROM-1) was used to remove non-specific signals. WAPL-1 was used for the estimation of progenitor zone length. All scripts related to image processing and data analysis can be found at Zenodo (https://doi.org/10.5281/zenodo.5704948 and https://doi.org/10.5281/zenodo.5704923). Primary and secondary antibodies are listed in table S10.

EdU pulse labeling

EdU labeling was carried out as previously described (*2*, *33*, *35*). Briefly, synchronized 24-hour post-L4 adult worms of the desired genotype were transferred to EdU-labeled plates. After exactly 30 min, gonads were dissected and stained with the desired primary and secondary antibodies, as described above. After overnight incubation with secondary antibodies, the gonads were washed three times for 10 min with PBST and then incubated with the EdU detection reaction mix for 30 min at room temperature using an EdU labeling kit (Invitrogen, catalog no. C10337). Gonads were then washed three times for 20 min with PBST to reduce the background signal for EdU labeling. Gonads were then incubated with DAPI and transferred to slides, as described above.

EdU labeling for meiotic output and progression analysis

Synchronized 24-hour post-L4 adult worms of the desired genotype were transferred to EdU-labeled plates. After 5 hours, worms were treated as follows: (i) For meiotic output, gonads were dissected immediately and stained with REC-8 and HIM-3 antibodies; or (ii) worms were transferred to OP50-seeded NGM plates and grown at 20°C for 48 hours, before gonads were dissected and stained with anti–HIM-3 and anti–CYE-1 antibodies. EdU staining was performed as described above.

Meiotic output

Two overlapping hyperstack images were captured to obtain coverage of all EdU-positive cells from the distal end of the gonad. All EdU/HIM-3–positive cells that were also REC-8 negative were marked using the "Multi-Point" tool in Fiji on every stack of hyperstack images. Duplicate counts were removed using a threshold of 15 with the duplicate_counter_removal plugin available at Zenodo (https://doi.org/10.5281/zenodo.5704948) to obtain the meiotic output after 5 hours of EdU labeling.

Meiotic progression

Three overlapping hyperstack images were captured to obtain coverage of all EdU-positive cells from the distal end of the gonad. CYE-1 and HIM-3 staining was used for the estimation of the progenitor zone length and the point of the meiotic entry. Cell diameters were marked and counted using the Multi-Point tool in Fiji, starting from the distal end of the germ line to determine (i) the progenitor zone and (ii) the position of the last EdU-positive cell from the beginning of the meiotic entry point.

PPM-1.D and CHK-2 bacterial expression and immunoprecipitation

cDNAs encoding *C. elegans* CHK-2 and PPM-1.D were cloned into homemade vectors (derivatives of pBR322) harboring kanamycin resistance to create the GST–CHK-2–(3×FLAG) and MBP-PPM1D-His10 fusion constructs. For protein production, the CHK-2 and PPM-1.D constructs were transformed into *E. coli* BL21(DE3) derivatives, and cells were grown at 37°C in terrific broth medium supplemented with kanamycin. When the *E. coli* cultures reached an optical density at 600 nm (OD_{600}) of 2, the temperature was reduced to 18°C, and after 1 hour, protein production was induced by the addition of 0.2 mM IPTG followed by incubation for 12 to 16 hours at 18°C. Cells expressing CHK-2 or PPM-1.D were then harvested by centrifugation, and cell pellets were resuspended in 2 ml of lysis buffer [50 mM sodium phosphate, 25 mM tris/HCl, 250 mM NaCl, 20 mM imidazole, 10% (v/v) glycerol, 0.05% (v/v) NP-40, and 5 mM β-mercaptoethanol (pH 7.5)] per gram of wet cell mass. Following ultrasonic lysis, insoluble material was removed by centrifugation at 21,000*g* for 10 min at 4°C. Lysates of MBP-PPM1D^{Truncation}-His10 and MBP-NRDE2ΔN-His10 were mixed with GST–CHK-2–(3×Flag) in a 1:50 ratio; 5 μl of MBP-PPM1D^{Truncation}-His10/MBP-NRDE2ΔN-His10 was mixed with 250 μl of GST–CHK-2–(3×Flag) and made up to 500 μl with lysis buffer. For MBP pull-down assays, 500 μl of supernatant was applied to 35 μl of

amylose resin (New England Biolabs, catalog no. E8021S) and incubated for 2 hours at 4°C. Subsequently, the resin was washed three times with 500 μl of lysis buffer. Proteins were eluted in 50 μl of lysis buffer supplemented with 20 mM maltose.

Yeast transformation and trichloroacetic acid protein precipitation

The yeast strain Mat-a was cotransfected with the PPM-1.D–LexA and PROM-1–HA vectors (table S9) using the lithium acetate method, as previously described (55), and colonies were selected on SC-Leu-Trp plates. After overnight growth, the culture medium was refreshed with 5 ml of synthetic medium–Leu–Trp to obtain an OD_{600} of 0.05, and cultures were grown until they reached an OD_{600} of 0.8. For proteasome inhibition, when cells reached an OD_{600} of around 0.6, MG132 was added to a final concentration of 10 μM, and then cultures were incubated until they reached an OD_{600} of 0.8. As the addition of MG132 reduces the cell division time, yeast samples treated with MG132 were processed separately to avoid the introduction of artifacts by keeping the other samples on ice.

A volume of 1.25-ml 100% ice-cold trichloroacetic acid (TCA; 20% final concentration) was added, and cells were harvested (1900g for 5 min at 4°C). Cells were washed with 1 ml of ice-cold 10% TCA and transferred into 1.5-ml Eppendorf tubes. Next, cells were pelleted (16,000g for 10 min at 4°C), and 200 μl of ice-cold 10% TCA and 200 μl of acid-washed glass beads were added to the pellet. Cells were disrupted using a FastPrep-24 5G instrument (MP Biomedicals) with three cycles (6.5 m/s, 45 s, and 5-min pause at 4°C). The supernatant was transferred to a fresh Eppendorf tube, and beads were washed three times with 200 μl of ice-cold 10% TCA; the washes were collected and combined with the supernatant and then centrifuged at 2400g for 10 min at 4°C. The pellet was resuspended in 200 μl of GSD buffer [40 nM tris/HCl (pH 6.8), 8 M urea, 5% SDS, 0.1 nM EDTA, and 2% (v/v) β-mercaptoethanol, with traces of bromophenol]. After the addition of 25 μl of unbuffered 1 M tris base, samples were boiled for 10 min and then centrifuged at 100g for 5 min. Samples (5 to 30 μl) were then separated by SDS–polyacrylamide gel electrophoresis.

Whole-worm extracts
Preselected L4 worms (200 per genotype per assay) were incubated at 20°C for 24 hours. Adults were then collected into 30 μl of TE buffer [10 mM tris and 1 mM EDTA (pH 8.0)] in a 1.5-ml Eppendorf tube. After the addition of 1× Laemmli buffer, worms were subjected to three cycles of freeze thawing.

Nuclei isolation and protein fractionation from large *C. elegans* cultures
Nuclei isolation and cellular fractionation were done as previously described (53). Briefly, large cultures of *C. elegans* were prepared by seeding 20 100-mm NGM plates with 1 ml of OP50 bacteria (obtained from centrifugation of 2 liters of overnight *E. coli* culture and resuspending into a final volume of 40 ml). Between 5000 and 6000 *C. elegans* embryos were added to each 100-mm plate and incubated at 20°C for 3 days. Young adult worms were collected and transferred to 50-ml tubes by washing the plates with M9 and leaving the tubes on a rack for 15 min to allow the worms to pellet by gravity; most of the M9 was then removed, and fresh M9 solution added. This washing step was repeated three times. The final wash was performed using NP buffer [10 mM Hepes-KOH (pH 7.6), 1 mM

EGTA, 10 mM KCl, 1.5 mM $MgCl_2$, 0.25 mM sucrose, 1 mM phenylmethylsulfonyl fluoride, and 1 mM dithiothreitol (DTT)] containing protease inhibitors (Roche, catalog no. 11836170001), and worms were pelleted by centrifugation at 600g for 2 min. A 1-ml sample of the worm pellet was used to isolate nuclei.

To isolate nuclei, worms were disrupted using a cooled metal Wheaton tissue grinder and the resulting suspension was filtered first with a 100-μm mesh and then with a 40-μm mesh. The filtered solution was centrifuged at 300g for 2 min at 4°C, and the supernatant from this step, which contains nuclei, was centrifuged at 2500g for 10 min at 4°C. The resulting supernatant was used as the cytosolic fraction, and the pellet contained germline nuclei. To separate the soluble and the DNA-bound protein nuclear fractions, we used a Qproteome Nuclear Protein Kit (QIAGEN, catalog no. 37582) according to the manufacturer's instructions.

Western blotting
Worm samples were prepared as follows: The cellular fraction (50 μg) was mixed with 1× Laemmli. For yeast protein extracts, the same amount of protein (based on their OD_{600} at the time of collection) was loaded into each well.

Samples were separated by electrophoresis in 1× SDS-tris-glycine buffer on precast 4 to 20% TGX gels (Bio-Rad). Proteins were transferred onto polyvinylidene difluoride membrane (activated in methanol for 20 s) for 1 hour at 4°C at 100 V in 1× tris-glycine buffer containing 20% methanol. Membranes were blocked for 1 hour in 1× tris-buffered saline containing 0.1% Tween 20 (TBST) and 5% milk; primary antibodies were added to the same buffer and incubated overnight at 4°C. Membranes were then washed in 1× TBST and incubated with the secondary antibody in TBST containing 5% milk for 1 hour at room temperature. After washing, membranes were incubated with WesternBright ECL substrate (Advansta) and developed using a ChemiDoc system (Bio-Rad). Primary and secondary antibodies are listed in table S10.

Mass spectrometry
Immunoprecipitated proteins were eluted from beads with three 20-μl volumes of 100 mM glycine (pH 2.0). Supernatants were collected, and the pH was adjusted to alkaline by addition of 1 M tris (pH 8.0). Disulfide bridges were reduced by adding DTT to a final concentration of 10 mM and incubating for 30 min at room temperature. Free thiols were alkylated with iodoacetamide at a concentration of 20 mM for 30 min at room temperature in the dark. Excess iodoacetamide was quenched with half of the amount of DTT used for reduction. Proteins were digested with 300 ng of trypsin overnight at 37°C. Digests were acidified by adding trifluoroacetic acid to a final concentration of 1%. Peptides were desalted on StageTips (56) and further purified according to the SP2 protocol by Waas *et al.* (57).

Peptide samples were separated on an Ultimate 3000 RSLC nanoflow chromatography system (Dionex, Thermo Fisher Scientific) using a precolumn for sample loading (Acclaim PepMap C18; 2 cm by 0.1 mm, 5 μm) and a C18 analytical column (Acclaim PepMap C18; 50 cm by 0.75 mm, 2 μm; both Dionex, Thermo Fisher Scientific) by applying a linear gradient from 2 to 35% solvent B (80% acetonitrile and 0.1% formic acid; solvent A, 0.1% formic acid) at a flow rate of 230 nl/min over 120 min. Eluting peptides were analyzed on a Q Exactive HF-X Orbitrap mass spectrometer (Thermo Fisher Scientific). For the data-dependent mode, survey scans were acquired in a mass

range of 375 to 1500 mass/charge ratio (m/z) with lock mass on, at a resolution of 120,000 at 200 m/z. The Automatic Gain Control (AGC) target value was set to 3×10^6 with a maximal injection time of 60 ms. The eight most intense ions were selected with isolation widths of 1.6 and 0.2 m/z offset and were fragmented in the Higher-energy C-trap dissociation (HCD) cell with a normalized collision energy of 28%. Spectra were recorded at a target value of 1×10^5 with a maximal injection time of 150 ms and a resolution of 30,000. Peptides with an unassigned charge state, a charge of +1 or a change of >+7 were excluded from fragmentation. The peptide match feature was set to preferred, and the exclude isotope feature was enabled. Selected precursors were dynamically excluded from repeated sampling for 30 s.

Raw data were processed using the MaxQuant software package 1.6.0.16 (www.maxquant.org/) (*58*) and searching against the UniProt reference database of *C. elegans* and a custom database of common contaminants. The search was performed with full tryptic specificity and a maximum of two missed cleavages. Carbamidomethylation of cysteine residues was set as fixed, and oxidation of methionine, phosphorylation of serine, threonine, and tyrosine, and N-terminal protein acetylation were set as variable modifications; all other parameters were set to default. The match between run feature and the search for second peptides was enabled. Results were filtered at the protein and peptide levels for a false discovery rate of 1%. The protein groups table was further processed in R (*59*). Reverse hits and contaminants, as well as hits with less than three valid Label-Free Quantitation (LFQ) values in at least one experimental group, were not considered for further analysis. Missing LFQ values were imputed by values from a normal distribution (with a downshift of −1.8 and a width of 0.3 SDs). LIMMA (*60*) was used to identify differentially enriched proteins at an adjusted $P < 5\%$ (Benjamini-Hochberg). As the three experimental replicates in each experiment were performed on different days, the replicate batch was defined as a random effect in the linear model.

Electron microscopy

chk-2::ha worms at 24 hours after L4 stage were incubated in 2% paraformaldehyde and 0.2% glutaraldehyde (both EM grade; EMS, USA) in 0.1 M 60 mM PIPES, 25 mM HEPES, 10 mM EGTA and 2 mM MgCl2 (PHEM buffer) (pH 7.0) for 2 hours at room temperature and then overnight at 4°C. The fixed gonads were embedded in 12% gelatin and cut into 1-mm³ blocks, which were infiltrated with 2.3 M sucrose overnight at 4°C. The blocks were mounted onto a Leica specimen carrier (Leica Microsystems, Austria) and frozen in liquid nitrogen. A Leica UCT/FCS cryo-ultramicrotome (Leica Microsystems, Austria) was used to cut the frozen blocks into ultrathin sections at a nominal thickness of 60 nm at −120°C. A mixture of 2% methylcellulose (25 centipoises) and 2.3 M sucrose in a 1:1 ratio was used as a pick-up solution. Sections were picked up onto 200-mesh Ni grids (Gilder Grids, UK) with a carbon-coated formvar film (Agar Scientific, UK). Fixation, embedding, and cryosectioning were as previously described (*61*).

Before immunolabeling, grids were placed onto plates with solidified 2% gelatin and warmed up to 37°C for 20 min to remove the pick-up solution. After quenching free aldehyde groups with glycine (0.1% for 15 min), a blocking step with 1% BSA (fraction V) in 0.1 M Sörensen phosphate buffer (pH 7.4) was performed for 40 min. Grids were then incubated in primary antibody (rabbit anti-HA polyclonal) diluted to 1:200 in 0.1 M Sörensen phosphate buffer overnight at 4°C, followed by a 2-hour incubation at room temperature in secondary antibody (goat anti-rabbit, coupled to 6-nm gold) diluted 1:20 in 0.1 M Sörensen phosphate buffer. Sections were stained with 4% uranyl acetate (Merck, Germany) and 2% methylcellulose at a 1:9 ratio (on ice). All labeling steps were done in a wet chamber. Sections were inspected using a FEI Morgagni 268D TEM (FEI, The Netherlands) operated at 80 kV. Electron micrographs were acquired using an 11-megapixel Morada charge-coupled device camera (Olympus-SIS, Germany). Primary and secondary antibodies are listed in table S6.

Quantification of gold particles

Pictures were stitched in Photoshop to assemble the nucleus. The nuclear diameter was measured vertically, horizontally, and across the two diagonals using ImageJ. From the four measurements, we extracted the radius, r_1, of the nucleus. To calculate the radius of the two circles inscribed in the nucleus and divide the nucleus into three areas of equal size, we used the following formulas: $r_2 = \sqrt{\frac{2}{3}}\, r_1$ (radius of the outermost inscribed circle) and $r_3 = \sqrt{\frac{1}{3}}\, r_1$ (radius of the outermost inscribed circle). The nuclear membrane was traced in ImageJ with broken lines, and the different zones were drawn using the line thickness function. Gold particles were manually counted in Photoshop images for each zone.

Line profile analysis

Using ImageJ, a line of 20 pixels in width and covering the diameter of a mitotic nucleus was created to measure the anti-HA antibody signal and added to the region of interest manager. At least 25 nuclei from the progenitor zone were processed this way. After collection of these line profiles, the line profiles were resampled with R software using the longest track as the reference and then averaged. Averaged line profiles were plotted using GraphPad Prism 6.

Quantification and statistical analysis

Statistical analyses were performed in GraphPad Prism 6. Datasets were tested for normal distribution; depending on outcome, populations were tested for significant differences using the two-tailed Fisher's exact test, Mann-Whitney test, or chi-square test, as appropriate for each dataset.

REFERENCES AND NOTES

1. E. J. A. Hubbard, T. Schedl, Biology of the *Caenorhabditis elegans* germline stem cell system. *Genetics* **213**, 1145–1188 (2019).
2. A. Mohammad, K. vanden Broek, C. Wang, A. Daryabeigi, V. Jantsch, D. Hansen, T. Schedl, Initiation of meiotic development is controlled by three post-transcriptional pathways in *Caenorhabditis elegans*. *Genetics* **209**, 1197–1224 (2018).
3. D. Hansen, L. Wilson-Berry, T. Dang, T. Schedl, Control of the proliferation versus meiotic development decision in the *C. elegans* germline through regulation of GLD-1 protein accumulation. *Development* **131**, 93–104 (2004).
4. S. L. Crittenden, K. A. Leonhard, D. T. Byrd, J. Kimble, Cellular analyses of the mitotic region in the *Caenorhabditis elegans* adult germ line. *Mol. Biol. Cell* **17**, 3051–3061 (2006).
5. K. J. Hillers, V. Jantsch, E. Martinez-Perez, J. L. Yanowitz, Meiosis. *WormBook* **2017**, 1–43 (2017).
6. J. L. Gerton, R. S. Hawley, Homologous chromosome interactions in meiosis: Diversity amidst conservation. *Nat. Rev. Genet.* **6**, 477–487 (2005).
7. J. Link, V. Jantsch, Meiotic chromosomes in motion: A perspective from *Mus musculus* and *Caenorhabditis elegans*. *Chromosoma* **128**, 317–330 (2019).

8. V. Jantsch, L. Tang, P. Pasierbek, A. Penkner, S. Nayak, A. Baudrimont, T. Schedl, A. Gartner, J. Loidl, *Caenorhabditis elegans* prom-1 is required for meiotic prophase progression and homologous chromosome pairing. *Mol. Biol. Cell* **18**, 4911–4920 (2007).

9. A. J. MacQueen, A. M. Villeneuve, Nuclear reorganization and homologous chromosome pairing during meiotic prophase require *C. elegans* chk-2. *Genes Dev.* **15**, 1674–1687 (2001).

10. A. M. Penkner, A. Fridkin, J. Gloggnitzer, A. Baudrimont, T. Machacek, A. Woglar, E. Csaszar, P. Pasierbek, G. Ammerer, Y. Gruenbaum, V. Jantsch, Meiotic chromosome homology search involves modifications of the nuclear envelope protein Matefin/SUN-1. *Cell* **139**, 920–933 (2009).

11. A. Sato, B. Isaac, C. M. Phillips, R. Rillo, P. M. Carlton, D. J. Wynne, R. A. Kasad, A. F. Dernburg, Cytoskeletal forces span the nuclear envelope to coordinate meiotic chromosome pairing and synapsis. *Cell* **139**, 907–919 (2009).

12. J. Link, D. Paouneskou, M. Velkova, A. Daryabeigi, T. Laos, S. Labella, C. Barroso, S. P. Piñol, A. Montoya, H. Kramer, A. Woglar, A. Baudrimont, S. M. Markert, C. Stigloher, E. Martinez-Perez, A. Dammermann, M. Alsheimer, M. Zetka, V. Jantsch, Transient and partial nuclear lamina disruption promotes chromosome movement in early meiotic prophase. *Dev. Cell* **45**, 212–225.e7 (2018).

13. A. Woglar, V. Jantsch, Chromosome movement in meiosis I prophase of *Caenorhabditis elegans*. *Chromosoma* **123**, 15–24 (2014).

14. Y. Kim, N. Kostow, A. F. Dernburg, The chromosome axis mediates feedback control of CHK-2 to ensure crossover formation in *C. elegans*. *Dev. Cell* **35**, 247–261 (2015).

15. M. Castellano-Pozo, S. Pacheco, G. Sioutas, A. L. Jaso-Tamame, M. H. Dore, M. M. Karimi, E. Martinez-Perez, Surveillance of cohesin-supported chromosome structure controls meiotic progression. *Nat. Commun.* **11**, 4345 (2020).

16. E. L. Stamper, S. E. Rodenbusch, S. Rosu, J. Ahringer, A. M. Villeneuve, A. F. Dernburg, Identification of DSB-1, a protein required for initiation of meiotic recombination in *Caenorhabditis elegans*, illuminates a crossover assurance checkpoint. *PLoS genetics* **9**, e1003679 (2013).

17. S. Rosu, K. A. Zawadzki, E. L. Stamper, D. E. Libuda, A. L. Resse, A. F. Dernburg, A. M. Villeneuve, The *C. elegans* DSB-2 protein reveals a regulatory network that controls competence for meiotic DSB formation and promotes crossover assurance. *PLoS genetics* **9**, e1003674 (2013).

18. L. Tang, T. Machacek, Y. M. Mamnun, A. Penkner, J. Gloggnitzer, C. Wegrostek, R. Konrat, M. F. Jantsch, J. Loidl, V. Jantsch, Mutations in *Caenorhabditis elegans* him-19 show meiotic defects that worsen with age. *Mol. Biol. Cell* **21**, 885–896 (2010).

19. B. Simon-Kayser, C. Scoul, K. Renaudin, P. Jezequel, O. Bouchot, J. Rigaud, S. Bezieau, Molecular cloning and characterization of FBXO47, a novel gene containing an F-box domain, located in the 17q12 band deleted in papillary renal cell carcinoma. *Genes Chromosomes Cancer* **43**, 83–94 (2005).

20. S. Nayak, F. E. Santiago, H. Jin, D. Lin, T. Schedl, E. T. Kipreos, The *Caenorhabditis elegans* Skp1-related gene family: Diverse functions in cell proliferation, morphogenesis, and meiosis. *Curr. Biol.* **12**, 277–287 (2002).

21. X. Le Guezennec, D. V. Bulavin, WIP1 phosphatase at the crossroads of cancer and aging. *Trends Biochem. Sci.* **35**, 109–114 (2010).

22. O. Crawley, C. Barroso, S. Testori, N. Ferrandiz, N. Silva, M. Castellano-Pozo, A. L. Jaso-Tamame, E. Martinez-Perez, Cohesin-interacting protein WAPL-1 regulates meiotic chromosome structure and cohesion by antagonizing specific cohesin complexes. *eLife* **5**, e10851 (2016).

23. W. Goodyer, S. Kaitna, F. Couteau, J. D. Ward, S. J. Boulton, M. Zetka, HTP-3 links DSB formation with homolog pairing and crossing over during *C. elegans* meiosis. *Dev. Cell* **14**, 263–274 (2008).

24. A. J. MacQueen, M. P. Colaiacovo, K. McDonald, A. M. Villeneuve, Synapsis-dependent and -independent mechanisms stabilize homolog pairing during meiotic prophase in *C. elegans*. *Genes Dev* **16**, 2428–2442 (2002).

25. K. Schild-Prufert, T. T. Saito, S. Smolikov, Y. Gu, M. Hincapie, D. E. Hill, M. Vidal, K. M. Donald, M. P. Colaiácovo, Organization of the synaptonemal complex during meiosis in *Caenorhabditis elegans*. *Genetics* **189**, 411–421 (2011).

26. A. R. Goloudina, E. Y. Kochetkova, T. V. Pospelova, O. N. Demidov, Wip1 phosphatase: Between p53 and MAPK kinases pathways. *Oncotarget* **7**, 31563–31571 (2016).

27. H. Jaiswal, J. Benada, E. Müllers, K. Akopyan, K. Burdova, T. Koolmeister, T. Helleday, R. H. Medema, L. Macurek, A. Lindqvist, ATM/Wip1 activities at chromatin control Plk1 re-activation to determine G2 checkpoint duration. *EMBO J.* **36**, 2161–2176 (2017).

28. P. Bork, N. P. Brown, H. Hegyi, J. Schultz, The protein phosphatase 2C (PP2C) superfamily: Detection of bacterial homologues. *Protein Sci.* **5**, 1421–1425 (1996).

29. M. Fiscella, H. Zhang, S. Fan, K. Sakaguchi, S. Shen, W. E. Mercer, G. F. Vande Woude, P. M. O'Connor, E. Appella, Wip1, a novel human protein phosphatase that is induced in response to ionizing radiation in a p53-dependent manner. *Proc. Natl. Acad. Sci.* **94**, 6048–6053 (1997).

30. M. R. Dello Stritto, B. Bauer, P. Barraud, V. Jantsch, DNA topoisomerase 3 is required for efficient germ cell quality control. *J. Cell Biol.* **220**, e202012057 (2021).

31. I. A. Shaltiel, L. Krenning, W. Bruinsma, R. H. Medema, The same, only different—DNA damage checkpoints and their reversal throughout the cell cycle. *J. Cell Sci.* **128**, 607–620 (2015).

32. M. Takekawa, M. Adachi, A. Nakahata, I. Nakayama, F. Itoh, H. Tsukuda, Y. Taya, K. Imai, p53-inducible wip1 phosphatase mediates a negative feedback regulation of p38 MAPK-p53 signaling in response to UV radiation. *EMBO J.* **19**, 6517–6526 (2000).

33. P. M. Fox, V. E. Vought, M. Hanazawa, M.-H. Lee, E. M. Maine, T. Schedl, Cyclin E and CDK-2 regulate proliferative cell fate and cell cycle progression in the *C. elegans* germline. *Development* **138**, 2223–2234 (2011).

34. B. Biedermann, J. Wright, M. Senften, I. Kalchhauser, G. Sarathy, M.-H. Lee, R. Ciosk, Translational repression of cyclin E prevents precocious mitosis and embryonic gene activation during *C. elegans* meiosis. *Dev Cell* **17**, 355–364 (2009).

35. Z. Kocsisova, A. Mohammad, K. Kornfeld, T. Schedl, Cell cycle analysis in the *C. elegans* germline with the thymidine analog EdU. *J Vis Exp* **2018**, 58339 (2018).

36. M. C. Zetka, I. Kawasaki, S. Strome, F. Muller, Synapsis and chiasma formation in *Caenorhabditis elegans* require HIM-3, a meiotic chromosome core component that functions in chromosome segregation. *Genes Dev.* **13**, 2258–2270 (1999).

37. A. Alpi, P. Pasierbek, A. Gartner, J. Loidl, Genetic and cytological characterization of the recombination protein RAD-51 in *Caenorhabditis elegans*. *Chromosoma* **112**, 6–16 (2003).

38. M. P. Colaiacovo, A. J. MacQueen, E. Martinez-Perez, K. M. Donald, A. Adamo, A. L. Volpe, A. M. Villeneuve, Synaptonemal complex assembly in *C. elegans* is dispensable for loading strand-exchange proteins but critical for proper completion of recombination. *Dev Cell* **5**, 463–474 (2003).

39. T. L. Gumienny, E. Lambie, E. Hartwieg, H. R. Horvitz, M. O. Hengartner, Genetic control of programmed cell death in the *Caenorhabditis elegans* hermaphrodite germline. *Development* **126**, 1011–1022 (1999).

40. A. Gartner, S. Milstein, S. Ahmed, J. Hodgkin, M. O. Hengartner, A conserved checkpoint pathway mediates DNA damage—Induced apoptosis and cell cycle arrest in *C. elegans*. *Mol. Cell* **5**, 435–443 (2000).

41. A. Adamo, A. Woglar, N. Silva, A. Penkner, V. Jantsch, A. la Volpe, Transgene-mediated cosuppression and RNA interference enhance germ-line apoptosis in *Caenorhabditis elegans*. *Proc. Natl. Acad. Sci. U.S.A.* **109**, 3440–3445 (2012).

42. Y. Aubert, S. Egolf, B. C. Capell, The unexpected noncatalytic roles of histone modifiers in development and disease. *Trends Genetics* **35**, 645–657 (2019).

43. V. Reiterer, K. Pawłowski, G. Desrochers, A. Pause, H. J. Sharpe, H. Farhan, The dead phosphatases society: A review of the emerging roles of pseudophosphatases. *FEBS J.* **287**, 4198–4220 (2020).

44. S. Pechackova, K. Burdova, L. Macurek, WIP1 phosphatase as pharmacological target in cancer therapy. *J. Mol. Med.* **95**, 589–599 (2017).

45. S. Brenner, The genetics of *Caenorhabditis elegans*. *Genetics* **77**, 71–94 (1974).

46. A. Paix, A. Folkmann, D. Rasoloson, G. Seydoux, High efficiency, homology-directed genome editing in *Caenorhabditis elegans* using CRISPR-Cas9 ribonucleoprotein complexes. *Genetics* **201**, 47–54 (2015).

47. A. D. Norris, H. M. Kim, M. P. Colaiacovo, J. A. Calarco, Efficient genome editing in *Caenorhabditis elegans* with a toolkit of dual-marker selection cassettes. *Genetics* **201**, 449–458 (2015).

48. E. Martinez-Perez, A. M. Villeneuve, HTP-1-dependent constraints coordinate homolog pairing and synapsis and promote chiasma formation during *C. elegans* meiosis. *Genes Dev.* **19**, 2727–2743 (2005).

49. V. Jantsch, P. Pasierbek, M. M. Mueller, D. Schweizer, M. Jantsch, J. Loidl, Targeted gene knockout reveals a role in meiotic recombination for ZHP-3, a Zip3-related protein in *Caenorhabditis elegans*. *Mol. Cell. Biol.* **24**, 7998–8006 (2004).

50. R. S. Kamath, M. Martinez-Campos, P. Zipperlen, A. G. Fraser, J. Ahringer, Effectiveness of specific RNA-mediated interference through ingested double-stranded RNA in *Caenorhabditis elegans*. *Genome Biol* **2**, research0002.1 (2000).

51. Y. Zhang, D. Chen, M. A. Smith, B. Zhang, X. Pan, Selection of reliable reference genes in *Caenorhabditis elegans* for analysis of nanotoxicity. *PLOS ONE* **7**, e31849 (2012).

52. T. D. Schmittgen, K. J. Livak, Analyzing real-time PCR data by the comparative CT method. *Nat. Protoc.* **3**, 1101–1108 (2008).

53. N. Silva, N. Ferrandiz, C. Barroso, S. Tognetti, J. Lightfoot, O. Telecan, V. Encheva, P. Faull, S. Hanni, A. Furger, A. P. Snijders, C. Speck, E. Martinez-Perez, The fidelity of synaptonemal complex assembly is regulated by a signaling mechanism that controls early meiotic progression. *Dev. Cell* **31**, 503–511 (2014).

54. J. Chen, A. Mohammad, N. Pazdernik, H. Huang, B. Bowman, E. Tycksen, T. Schedl, GLP-1 Notch-LAG-1 CSL control of the germline stem cell fate is mediated by transcriptional targets lst-1 and sygl-1. *PLOS Genet.* **16**, e1008650 (2020).

55. C. Kraft, M. Kijanska, E. Kalie, E. Siergiejuk, S. S. Lee, G. Semplicio, I. Stoffel, A. Brezovich, M. Verma, I. Hansmann, G. Ammerer, K. Hofmann, S. Tooze, M. Peter, Binding of the Atg1/ULK1 kinase to the ubiquitin-like protein Atg8 regulates autophagy. *EMBO J.* **31**, 3691–3703 (2012).

56. J. Rappsilber, M. Mann, Y. Ishihama, Protocol for micro-purification, enrichment, pre-fractionation and storage of peptides for proteomics using StageTips. *Nat. Protoc.* **2**, 1896–1906 (2007).

57. M. Waas, M. Pereckas, R. A. Jones Lipinski, C. Ashwood, R. L. Gundry, SP2: Rapid and automatable contaminant removal from peptide samples for proteomic analyses. *J. Proteome Res.* **18**, 1644–1656 (2019).

58. J. Cox, M. Mann, MaxQuant enables high peptide identification rates, individualized p.p.b.-range mass accuracies and proteome-wide protein quantification. *Nat Biotechnol* **26**, 1367–1372 (2008).

59. R Core Team, R: A Language and Environment for Statistical Computing (2021).

60. M. E. Ritchie, B. Phipson, D. Wu, Y. Hu, C. W. Law, W. Shi, G. K. Smyth, *limma* powers differential expression analyses for RNA-sequencing and microarray studies. *Nucleic Acids Res.* **43**, e47 (2015).

61. K. T. Tokuyasu, A technique for ultracryotomy of cell suspensions and tissues. *J. Cell Biol.* **57**, 551–565 (1973).

62. A. F. Dernburg, K. McDonald, G. Moulder, R. Barstead, M. Dresser, A. M. Villeneuve, Meiotic recombination in *C. elegans* initiates by a conserved mechanism and is dispensable for homologous chromosome synapsis. *Cell* **94**, 387–398 (1998).

63. E. R. Hofmann, S. Milstein, S. J. Boulton, M. Ye, J. J. Hofmann, L. Stergiou, A. Gartner, M. Vidal, M. O. Hengartner, *Caenorhabditis elegans* HUS-1 is a DNA damage checkpoint protein required for genome stability and EGL-1-mediated apoptosis. *Curr. Biol.* **12**, 1908–1918 (2002).

64. R. Clifford, M. L. Lee, S. Nayak, M. Ohmachi, F. Giorgini, T. Schedl, FOG-2, a novel F-box containing protein, associates with the GLD-1 RNA binding protein and directs male sex determination in the *C. elegans* hermaphrodite germline. *Development* **127**, 5265–5276 (2000).

65. A. E. Friedland, Y. B. Tzur, K. M. Esvelt, M. P. Colaiácovo, G. M. Church, J. A. Calarco, Heritable genome editing in *C. elegans* via a CRISPR-Cas9 system. *Nat Methods* **10**, 741–743 (2013).

66. C. Frokjaer-Jensen, M. W. Davis, C. E. Hopkins, B. J. Newman, J. M. Thummel, S.-P. Olesen, M. Grunnet, E. M. Jorgensen, Single-copy insertion of transgenes in *Caenorhabditis elegans*. *Nat. Genet.* **40**, 1375–1383 (2008).

67. D. J. Dickinson, J. D. Ward, D. J. Reiner, B. Goldstein, Engineering the *Caenorhabditis elegans* genome using Cas9-triggered homologous recombination. *Nat. Methods* **10**, 1028–1034 (2013).

68. P. Pasierbek, M. Jantsch, M. Melcher, A. Schleiffer, D. Schweizer, J. Loidl, A *Caenorhabditis elegans* cohesion protein with functions in meiotic chromosome pairing and disjunction. *Genes Dev.* **15**, 1349–1360 (2001).

69. T. M. Brodigan, J. Liu, M. Park, E. T. Kipreos, M. Krause, Cyclin E expression during development in *Caenorhabditis elegans*. *Dev. Biol.* **254**, 102–115 (2003).

70. M. E. Hurlock, I. Čavka, L. E. Kursel, J. Haversat, M. Wooten, Z. Nizami, R. Turniansky, P. Hoess, J. Ries, J. G. Gall, O. Rog, S. Köhler, Y. Kim, Identification of novel synaptonemal complex components in *C. elegans*. *J. Cell Biol.* **219**, e201910043 (2020).